Experimental and Theoretical Studies of a
35 GHz Cyclotron Autoresonance Maser Amplifier

DiRienzo, A. C.*; Bekefi, G.; Chen, C.;
and Wurtele, J.

November 1990

Department of Physics
Research Laboratory of Electronics
and
Plasma Fusion Center
Massachusetts Institute of Technology
Cambridge, Massachusetts 02139

*present address: HQDA, OASA (RDA), Attn: SARD-DO, Washington, D.C.,
20310-0103

Experimental and Theoretical Studies of a 35GHz Cyclotron Autoresonance Maser Amplifier*

A.C. DiRienzo[†], G. Bekefi, C. Chen and J.S. Wurtele

Department of Physics

Research Laboratory of Electronics

and

Plasma Fusion Center

Massachusetts Institute of Technology

Cambridge, Massachusetts 02139

ABSTRACT

Experimental and theoretical studies of a cyclotron autoresonance maser (CARM) amplifier are reported. The measurements are carried out at a frequency of 35GHz using a mildly relativistic electron beam (1.5 MeV, 130A, 30 ns) generated by a field emission electron gun followed by an emittance selector that removes the outer, hot electrons. Perpendicular energy is imparted to the electrons by means of a short bifilar helical wiggler. The entire system is immersed in a uniform axial magnetic field of 6–8 kG. With an input power of 17 kW at 35 GHz from a magnetron driver, the saturated power output is 12 MW in the lowest TE_{11} mode of a circular waveguide, corresponding to an electronic efficiency of 6.3%. The accompanying linear growth rate is 50 dB/m. When the system operates in the superradiant mode (in the absence of the magnetron driver) excitation of multiple waveguide modes is observed. A three-dimensional simulation code that has been developed to investigate the self-consistent interaction of the copropagating electromagnetic waveguide mode and the relativistic electron beam is in good agreement with the experimental observations.

1

I. INTRODUCTION

The cyclotron autoresonance maser (CARM) has received considerable interest in recent years as a potential source of high power microwave and millimeter wavelength electromagnetic radiation. It has been subjected to extensive theoretical studies and numerical simulations[1-12]. However, unlike the closely related gyrotron and free electron laser, the capabilities of the CARM as a source of coherent radiation have not yet been tested extensively in the laboratory. Thus, at the present time there are several experiments in the planning stage[13-17] and a small number of oscillator studies[18,19,20]. This paper is concerned exclusively with the properties of a CARM as a single pass amplifier. Preliminary studies on this device were reported earlier[21.22].

The emission from the CARM occurs through the resonant interaction between the Doppler upshifted cyclotron wave on the electron beam,

$$\omega = l\Omega_0/\gamma + k_z v_z \tag{1}$$

and a co-propagating electromagnetic waveguide mode

$$\omega^2 = k_z^2 c^2 + \omega_c^2 . \tag{2}$$

Here ω and k_z are the frequency and axial wave number, respectively; $\Omega_0 = eB_z/m_0 c$ is the nonrelativistic cyclotron frequency associated with the axial guide magnetic field B_z; $l = 1, 2, 3...$ is the harmonic number and $\gamma = [1 - (v_z^2 + v_\perp^2)/c^2]^{-\frac{1}{2}}$ is the relativistic energy factor; ω_c is the cutoff frequency of the waveguide mode in question.

3

Equation (1) can be rearranged to yield the well-known resonant condition

$$\omega = \frac{l\Omega_0}{\gamma(1 - \beta_z/\beta_{ph})} \qquad (3)$$

where $\beta_z = v_z/c$ and $\beta_{ph} = \omega/k_z c$ is the normalized phase velocity of the wave. It is seen from Eq. (3) that when the ratio (β_z/β_{ph}) approaches unity very high frequencies ω can be achieved using relatively modest axial magnetic fields B_z. Therein lies the attractiveness of the CARM as compared with the gyrotron, for which, typically $\gamma \simeq 1$, $(\beta_z/\beta_{ph}) \ll 1$ and $\gamma\omega/\Omega_0 \simeq 1$. By way of contrast, our CARM experiments have $B_z \simeq 5.4$ kG, $\gamma = 3.94$, $\beta_z \simeq 0.94$, $\beta_{ph} = 1.056$ and, thus, $\gamma\omega/\Omega_0 \simeq 9.1$.

Maximum gain of the CARM instability occurs near phase velocity synchronism of the waves described by Eqs. (1) and (2). Elimating the wave number k_z yields the radiation frequency,

$$\omega = l\Omega_0 \frac{\gamma_z^2}{\gamma} \left\{ 1 \pm \beta_z \left[1 - \left(\frac{\omega_c \gamma}{l\Omega_0 \gamma_z} \right)^2 \right]^{\frac{1}{2}} \right\}, \qquad (4)$$

where $\gamma_z = (1 - \beta_z^2)^{-\frac{1}{2}}$ and the positive sign refers to the sought after Doppler upshifted mode of operation. We note that the Doppler downshifted "gyrotron" mode (with the negative sign) can become absolutely unstable[23], and if excited may cause serious deterioration of the CARM amplifier performance.

This paper describes an experimental and theoretical study of a CARM amplifier operating in the fundamental $l = 1$ mode, with the view of using this or a similar device as a potential driver of the Berkeley- Haimson high gradient acceleration (HGA) test stand[24]. The experiments are performed at a radiation frequency of 35 GHz using a

mildly relativistic electron beam with an energy of 1.5 MeV, a beam current of 130 A and a pulse duration of $\sim$ 30 ns. The beam is generated from a field emission (explosive emission) cathode and then propagates through an emittance selector that removes the outermost hot electrons. Perpendicular energy is imparted to the electrons at the input to the CARM by means of a bifilar helical magnetic wiggler.

The linear growth rate of the CARM instability is measured to be $\sim$ 50 dB/m, resulting in a saturated power output of $\sim$ 12 MW and an electronic efficiency of 6.3%. Our amplifier studies are conducted with an input electromagnetic wave supplied by a high power magnetron driver and also in the superradiant regime where the wave grows out of noise. In the former situation the radiation is confined to the lowest TE_{11} mode of the circular waveguide. However, in the latter case there is evidence of excitation of multiple waveguide modes.

In Sec. II we describe the experimental arrangement. In Sec. III we summarize the theoretical results and the simulations used to interpret the measurements which are described in Sec. IV. A discussion is presented in Sec. V.

II. THE EXPERIMENT

1. The Electron Beam

A schematic of the CARM is shown in Fig. 1(a). The accelarating potential for the maser is supplied by a Marx generator (Physics International Pulserad 110A) capable of supplying a 1.5 MeV, 20 kA, 40 ns pulse to a 75 Ω matched load. The electron beam is generated by a field emission (explosive emission) gun shown in Fig. 1(b) composed of a hemispherical graphite cathode and a conical anode[25] which also acts as an emittance selector. Typical oscilloscope traces of the voltage (corrected for inductive effects[26]), the current and radiation intensity are illustrated in Fig. 2.

The entire 2 m long system (including the gun) is immersed in a uniform axial magnetic field B_z of up to 8 kG. It is generated by a solenoid energized by a capacitor bank that delivers a sinusoidal current pulse of $\sim$ 16 ms duration.

Of the 20 kA of current available from the electron gun, only a small fraction I_b passes through the graphite anode which also acts as the emittance selector [see Fig. 3(a)]. The anode tube scrapes off the outer hot electrons, leaving a relatively cool inner core for use in the CARM interaction. Moreover, a measurement of the transmitted current I_b as a function of the axial magnetic field B_z at the emittance selector permits a determination of the normalized beam brightness B_n and the normalized rms beam emittance ϵ_n (rms) by means of the relations [27],

$$B_n = \frac{\pi^2 I_b}{(\gamma_z \beta_z)^2 (\delta^4 V)} = \frac{2 I_b}{9 \epsilon_n^2 (rms)} \quad . \tag{5a}$$

6

Here the phase space volume $\delta^4 V$ is given by

$$\delta^4 V = \pi^2 r_b^4 \Omega_0^2 / 6c^2 \gamma^2 \ . \tag{5b}$$

With r_b as the radius of the emittance selector. It follows from Eqs. 5(a) and 5(b) that for a constant brightness gun, the transmitted current I_b is proportional to B_z^2, a result which is in agreement with the measurements shown in Fig. 3(b).

Table I illustrates the results of such measurements for the case of emittance selectors having radii of 0.076 cm and 0.318 cm, respectively. In addition to B_n and ϵ_n (rms) the table also lists the normalized axial momentum spread $\Delta p_z / m_0 c$ and the corresponding energy spread $\Delta \gamma_z / \gamma_z$ of our beam, as derived from ϵ_n. It is noteworthy that the smaller radius beam is of high quality, albeit of low current. Being desirous of high power output from the CARM, we chose the higher current, less good beam in all the measurements described henceforth. Such a choice is not immediately obvious, since the CARM efficiency and power output are known to depend quite sensitively on beam quality. However, we were fortunate in our decision as the subsequent computer simulations described in Sec. III have shown.

2. The Magnetic Wiggler

Downstream from the emittance selector, a bifilar helical magnetic wiggler (see Fig. 1a) imparts tranverse velocity $v_\perp$ to the electron beam. The wiggler consists of current carrying bifilar helical windings and is energized by current from a capacitor bank with time constant ~ 100 μs. The wiggler field is gradually tapered from zero

7

field to its desired maximum value and then abruptly terminated by a copper shorting ring. The tapering is achieved[28,29] by means of nichrome wire resistive rings, two per period, and extending over the full 6 period wiggler length. The measured field profile is illustrated in Fig. 4(a).

Prior to taking radiation measurements, an axially moveable current collecting probe is used to measure the electron beam current at any axial position z in the wiggler and CARM interaction regions. A 30% current loss is observed as the beam traverses the wave launcher and wiggler regions (see Fig. 1). However, no significant current loss occurs within the CARM interaction region itself.

A piece of thermal paper attached to the current collector acts as a witness plate. It is used in two ways. First, to align the beam concentrically in the evacuated cylindrical drift tube and solenoid, and secondly to observe the helical precession of the beam when the magnetic wiggler field is turned on. Figure 4(b) illustrates the burn marks produced by the beam as the probe is moved axially within the wiggler field. The radial excursion of the beam, r, from the axis is a measure of the tranverse velocity imparted by the wiggler; typically, $\alpha \equiv v_\perp/v_z = k_w r \simeq 0.3$ for our experiments.

Magnetic wigglers[30,31] immersed in a uniform axial magnetic field normally operate in one of two regimes, depending whether the electron cyclotron wavelength is smaller or larger than the wiggler period, that is,

$$k_w v_z \gtrless \Omega_0/\gamma .$$

(6)

It is not known or fully understood which of these two regimes is preferable for the

purpose of spinning up the electrons. For that reason we constructed and used two wigglers, one operating in regime I characterized by $k_w v_z > \Omega_0/\gamma$, and the other operating in regime II for which $k_w v_z < \Omega_0/\gamma$. Figure 5 and Table II give the characteristics of the two wigglers used.

A transport code [32] that models single particle motions in the combined solenoidal and wiggler magnetic fields, but neglects both radiation and space-charge has been used to study the particle dynamics. In the numerical computations, the Biot-Savart law is used to generate the magnetic fields from the actual currents in the windings. The beam is treated as a group of up to 1024 macroparticles with various possible initial phase space distributions.

In this manner one obtains information about the average perpendicular energy of the macroparticles as defined by the parameter $\alpha = \beta_\perp/\beta_z$, the average pitch angle spread specified in terms of $\Delta\gamma_z/\gamma_z$, and the beam profile at any position z within the wiggler or CARM interaction regions. Figures 6(a) and 6(b) illustrate the dependence of α and $\Delta\gamma_z/\gamma_z$ on the axial position z for the experimental parameters of our CARM. In Fig. 6(a) we see that for the parameters chosen, there is virtually no decrease in the value of $\beta_\perp/\beta_z$ as the electrons pass from the wiggler to the CARM region. Figure 6(b) shows that there is only a small increase in temperature caused by the electron beam traversing the wiggler (the value of $\Delta\gamma_z/\gamma_z = 0.044$ at the input to the wiggler, $z = 0$, represents the value determined from the emittance measurements summarized in Table I). Figure 7 shows the simulated beam at three successive distances just beyond the downstream wiggler end. The three spots are separated in z by one third of a

9

cyclotron wavelength ($\lambda_c = 2\pi v_z \gamma / \Omega_0 = 7.3$ cm). A notch in the particle distribution of Fig. 7 shows that beam body rotation is minimal. The average electron Larmor radius $r_L = 0.35$ cm and there is a guiding center offset $r_g = 0.16$ cm. The latter, undesirable effect can lead to loss in CARM growth rate and efficiency. To correct for the offset, some magnetic steering to again center the beam is performed in the experiments.

The foregoing illustrations refer to type I wiggler orbits; similar results are obtained for the type II orbits. However, it is important to point out that the ultimate values of α, $\Delta \gamma_z / \gamma_z$, the shape of the beam profile and the magnitude of the beam offset as one enters the CARM region depend sensitively on the wiggler parameters, wiggler uptaper and wiggler length[33]. This is particularly true as one approaches the resonance condition $k_z v_z = \Omega_0 / \gamma$. For example, the transport code shows that a poor choice of wiggler parameters can easily lead to an almost total loss of perpendicular beam velocity when the electrons traverse the wiggler terminating ring.

3. Radiation Transport and Diagnostics

The stainless steel drift tube has an internal radius of 0.79 cm and acts as a cylindrical waveguide whose fundamental TE_{11} mode has a cutoff frequency of 11.16 GHz. A schematic diagram of the entire transport and detection system is given in Fig. 8(a).

A high power magnetron ($\sim$ 50 kW) operating at 34.73 GHz is the input power source for the CARM. The launcher [see Fig. 8(b)] consists of a section of circular waveguide of radius 0.32 cm into which the RF power is coupled from a standard Ka-band rectangular waveguide. This section of circular waveguide supports only the fundamental TE_{11} mode at our operating frequency. Its radius is then adiabatically uptapered to the radius of the drift tube. A linearly polarized wave is thereby injected into the interaction region.

The output power from the CARM is sent by means of a conical horn [see Fig. 8(c)] into a reflection free "anechoic chamber". The vacuum interface between the transmitting horn and chamber is provided by a TPX plastic[34] window whose power reflectivity is measured to be $\sim 2 \times 10^{-5}$. A small fraction of the radiated power is then collected by a receiving rectangular horn placed in the far (Fraunhoffer) field of the transmitter. Subsequently, the power is further reduced by means of precision calibrated attenuators and injected into a narrow band pass (± 0.75 GHz) filter. The power level is finally determined from the response of a calibrated crystal detector. The absolute CARM output power is obtained by a substitution method: the wiggler is turned off

11

and the transmitted power from the device (in the absence of the CARM amplification process) is determined in terms of the known input power from the magnetron. The measurement is then repeated with the CARM interaction in place.

In order to assure ourselves that the radiation is predominantly in the TE_{11} mode, the far field radiation pattern of the conical horn has been determined both in the absence and presence of the CARM interaction. The results of these measurements are illustrated in Fig. 9. The good agreement with a Kirchhoff-type diffraction theory[35] shown by the solid curve assures one that the fundamental waveguide mode is excited.

The spatial growth rate of the electromagnetic wave is determined from the measurement of the output power as a function of the length of the interaction region. This length is varied by changing the distance that the electron beam is allowed to propagate in the drift tube. The application of a strong transverse magnetic field generated by a movable kicker magnet[29] is sufficient to deflect the electrons into the waveguide wall, and thus terminate the interaction at that point.

The RF launcher injects linearly polarized electromagnetic radiation, half of which, because of the wrong handedness, does not participate in the CARM interaction. The remaining circurlarly polarized wave with the correct handedness is amplified and eventually emanates from the conical horn as circularly polarized radiation. This has been verified by rotating the pick up antenna 90° relative to the direction of polarization of the incident wave from the magnetron.

III. THEORY

A three-dimensional simulation code has been developed at MIT to simulate the self-consistent interaction of the electromagnetic wave and relativistic electron beam in CARM amplifiers. The code[7,9] which has been benchmarked against linear theory, can handle single TE (TM) mode, multiple TE and TM modes, cyclotron harmonics, magnetic field tapering, momentum spread, waveguide loss, various initial beam loadings, etc.

For a CARM amplifier operating with a single TE_{mn} mode, the radiation field can be expressed as

$$\vec{E}_t(r,\theta,z,t) = \frac{1}{2}E(z)\vec{e}_z \times \nabla_t J_m(k_\perp r)e^{i(m\theta-\omega t)} + \text{c.c.} ,$$

$$\vec{B}_t(r,\theta,z,t) = \frac{1}{2}\left(\frac{ic}{\omega}\right)\frac{dE(z)}{dz}\nabla_t J_m(k_\perp r)e^{i(m\theta-\omega t)} + \text{c.c.} , \qquad (7)$$

$$B_z(r,\theta,z,t) = \frac{1}{2}\left(\frac{ick_\perp^2}{\omega}\right)E(z)J_m(k_\perp r)e^{i(m\theta-\omega t)} + \text{c.c.} ,$$

where $\nabla_t = \vec{e}_r\partial/\partial r + (\vec{e}_\theta/r)\partial/\partial\theta$, $\omega = 2\pi f$ is the (angular) operating frequency, $E(z)$ is a z-dependent wave amplitude, $J_m(x)$ is the first-kind Bessel function of order m, $k_\perp = \nu/r_w$ is the transverse wavenumber associated with the TE_{mn} mode, and ν is the nth zero of $J'_m(x) = dJ_m(x)/dx$.

It is convenient to introduce the slowly varying normalized wave amplitude $A(z)$ and phase shift $\delta(z)$ defined by

$$E(z) = \frac{m_0 c^2}{e}\left(\frac{\omega}{ck_\perp}\right)A(z)e^{i[k_z z+\delta(z)]} . \qquad (8)$$

13

The dynamics of each individual particle is described by the particle energy $\gamma m_0 c^2$, axial momentum $p_z = \gamma m_0 v_z$, and phase ψ, assuming the guiding-center variables r_g and θ_g as constants (Fig. 10). Making use of the approximations $dA/dz \ll k_z A$ and $d\delta/dz \ll k_z \delta$ and neglecting $d^2 A/dz^2$, etc., it can be shown from the Lorentz force law and Maxwell equations that the self-consistent CARM amplifier equations for the single TE_{mn} mode at harmonic cyclotron frequency $l\Omega_c/\gamma$ can be expressed in the dimensionless form

$$\frac{d\gamma}{d\hat{z}} = -\frac{\hat{p}_\perp}{\hat{p}_z} X(r_L, r_g) A \cos\psi \,, \tag{9}$$

$$\frac{d\hat{p}_z}{d\hat{z}} = -\frac{\hat{p}_\perp}{\hat{p}_z} X(r_L, r_g) \left[\left(\frac{1}{\beta_{ph}} + \frac{d\delta}{d\hat{z}} \right) A \cos\psi + \frac{dA}{d\hat{z}} \sin\psi \right] \,, \tag{10}$$

$$\frac{d\psi}{d\hat{z}} = \frac{1}{\beta_{ph}} + \frac{d\delta}{d\hat{z}} - \frac{\gamma}{\hat{p}_z} + \frac{l\hat{\Omega}_0}{\hat{p}_z}$$

$$+ \frac{l}{\hat{p}_z \hat{p}_\perp} W(r_L, r_g) \left\{ \left[\gamma - \hat{p}_z \left(\frac{1}{\beta_{ph}} + \frac{d\delta}{d\hat{z}} \right) \right] A \sin\psi + \hat{p}_z \frac{dA}{d\hat{z}} \cos\psi \right\} \,, \tag{11}$$

$$\frac{dA}{dz} = g \left\langle X(r_L, r_g) \frac{\hat{p}_\perp}{\hat{p}_z} \cos\psi \right\rangle \,, \tag{12}$$

$$\frac{d\delta}{dz} = -\frac{g}{A} \left\langle X(r_L, r_g) \frac{\hat{p}_\perp}{\hat{p}_z} \sin\psi \right\rangle \,, \tag{13}$$

where

$$g = \frac{4(\beta_{ph}^2 - 1)}{\beta_{ph}(\nu^2 - m^2) J_m^2(\nu)} \left(\frac{I_b}{I_A} \right) \tag{14}$$

14

is a dimensionless coupling constant, and

$$X(r_L, r_g) = J_{l-m}(k_\perp r_g) J_l'(k_\perp r_L) , \tag{15}$$

$$W(r_L, r_g) = l J_{l-m}(k_\perp r_g) J_l(k_\perp r_L)/k_\perp r_L \tag{16}$$

are geometric factors. A detailed derivation of Eqs. (9-13) can be found in Refs. (7) and (9). In Eqs. (9-16), $\psi = k_z z + \delta(z) - \omega t + l\phi - (l-m)\theta_g + (l-2m)\pi/2$; $\hat{z} = \omega z/c$ is the normalized axial distance; $\phi = \tan^{-1}(p_x/p_y)$, $\hat{\Omega}_0 = \Omega_0/\omega$ is the normalized nonrelativistic cyclotron frequency $\hat{p}_z = p_z/m_0 c = \gamma\beta_z$, $\hat{p}_\perp = p_\perp/m_0 c = \gamma\beta_\perp$, and $\gamma = (1 + \hat{p}_z^2 + \hat{p}_\perp^2)^{1/2}$ are, respectively, the normalized axial and transverse momentum components and relativistic mass factor of the beam electron; I_b is the beam current; $I_A = m_0 c^3/e \simeq 17$ kA is the Alfvén current; $\beta_{ph} = \omega/ck_z = (1 - c^2 k_\perp^2/\omega^2)^{-1/2}$ is the normalized phase velocity of the vacuum TE_{mn} waveguide mode; $r_L = p_\perp/m_0\Omega_0$ is the electron Larmor radius. In Eqs. (12) and (13), $< f >= N^{-1}\sum_{i=1}^{N} f_i$ denotes the ensemble averaging over the particle distribution, and typically more than 1024 particles are used in the simulations. The rf power flow over the cross section of the waveguide for the TE_{mn} mode, $P(z) = (c/4\pi)\int_{\pi r_w^2}(\vec{E} \times \vec{B})_z d\sigma$, is related to the normalized wave amplitude $A(z)$ by the expression

$$P(\hat{z}) = \frac{1}{8}\left(\frac{m_0^2 c^5}{e^2}\right)\frac{\beta_{ph}(\nu^2 - m^2)J_m^2(\nu)}{(\beta_{ph}^2 - 1)}A^2(\hat{z}) , \tag{17}$$

where $m_0^2 c^5/e^2 \simeq 8.7$ GW. It is readily shown from Eqs. (9), (12), and (17) that

$$P + \frac{I_b}{e} < \gamma > m_0 c^2 = \text{const.} , \tag{18}$$

corresponding to the conservation of total power flow through the waveguide.

To benchmarked the simulation code, a linear analysis of the cyclotron resonance maser interaction has been carried out using the Maxwell-Vlasov equations and Laplace transform. For the CARM interaction of a cold, thin $(k_\perp r_g \ll 1)$, azimuthally symmetric electron beam with the single TE_{mn} mode at harmonic cyclotron frequency $l\Omega_c/\gamma$, the Laplace transform of the wave amplitude $E(z)$ to leading order in $c^2 k_\perp^2/(\omega - l\Omega_0/\gamma - k_z v_z)^2$ is found to be approximately

$$\left[\left(s^2 - k_\perp^2 + \frac{\omega^2}{c^2}\right) + \frac{\epsilon k_\perp^2(\omega^2 + c^2 s^2)}{(\omega - l\Omega_0/\gamma + iv_z s)^2}\right]\hat{E}(s) = \left[s + \frac{i\epsilon k_\perp^2 v_z \omega}{(\omega - l\Omega_0/\gamma + iv_z s)^2}\right]E(0) . \quad (19)$$

Here, $dE(0)/dz = 0$ has been assumed, $s = ik_z$ is the Laplace transform variable, and

$$\epsilon = \frac{4\beta_\perp^2}{\gamma\beta_z}\left(\frac{I_b}{I_A}\right)\frac{X^2(r_L, r_g)}{(\nu^2 - m^2)J_m^2(\nu)} \quad (20)$$

is a dimensionless coupling constant. Therefore, the rf power gain including launching losses can be obtained by the inverse Laplace transform of $\hat{E}(s)$, i.e.,

$$\frac{P(z)}{P(0)} = \left|\frac{E(z)}{E(0)}\right|^2 = \left|\frac{1}{2\pi i}\int_{\sigma-i\infty}^{\sigma+i\infty}\frac{\hat{E}(s)}{E(0)}e^{sz}ds\right|^2 . \quad (21)$$

Note that the poles in the integrand in Eq. (21) correspond to the solutions of the algebraic equation

$$k_z^2 + k_\perp^2 - \frac{\omega^2}{c^2} = \frac{\epsilon k_\perp^2(\omega^2 - c^2 k_z^2)}{(\omega - l\Omega_0/\gamma - k_z v_z)^2} , \quad (22)$$

which is the usual dispersion relation for the single TE_{mn} mode, to leading order in $c^2 k_\perp^2/(\omega - l\Omega_0/\gamma - k_z v_z)^2$.

Figure 11 depicts typical dependence of rf power $P(z)$ on the interaction length z for the TE_{11} mode obtained from the numerical sumulations and linear theory. Here,

16

the system parameters are frequency $f = 34.7$ GHz, waveguide radius $r_w = 0.793$ cm, axial magnetic field $B_0 = 5.62$ kG, beam current $I_b = 128$ A, initial pitch angle $\alpha = 0.27$ rad, energy spread $\Delta\gamma_z/\gamma_z = 0$, and guiding center radius $r_g = 0$, corresponding to the TE$_{11}$ mode in resonance with the beam mode at the fundamental cyclotron frequency $(l = 1)$. In Fig. 11, the solid curve shows the simulation result obtained by solving numerically Eqs. (9-13), while the dashed curve is obtained analytically from Eqs. (19) and (21). It is evident in Fig. 11 that there is good agreement between the simulations and theory in the linear regime.

Figure 12(a) illustrates the dependence of the saturated efficiency and linear growth rate on energy spread $\Delta\gamma_z/\gamma_z$ as derived from our simulation. When the energy spread is 0.044 typical of our CARM, the predicted efficiency is seen to be $\sim 6\%$ and the growth rate ~ 45 dB/m, values that are in good agreement with measurements described in the following section. Figure 12(b) presents the computed power output as a function of frequency around the nominal 35 GHz design frequency. Thus, it illustrates the CARM performance as a function detuning.

IV. GROWTH RATE AND SATURATION MEASUREMENTS

1. Amplifier studies

The radiation output at the fixed magnetron input frequency of 34.73 GHz and fixed input power of 18 kW is optimized by varying both the guide B_z and wiggler fields B_w. Figure 13(a) shows how the output intensity varies with B_z at constant B_w; and Fig. 13(b) shows how it varies with B_w at constant B_z. Once the optimal values of B_z and B_w are determined, the radiation intensity is then measured as a function of the CARM interaction length z. This is done by a movable magnetic kicker magnet as described at the end of Sec. II. The results of these measurements are depicted in Fig. 14 for both wigglers used (see Table I). The solid lines are from simulation which also takes into account the attenuation suffered by the radiation in its passage through the stainless steel waveguide (~ 0.6 dB/m). The overall agreement between experiment and theory is good.

2. Superradiant studies

We have also carried out a series of measurements of the superradiant emission from the CARM amplifier. This is done by simply turning off the magnetron driver and allowing the radiation to grow out of spontaneously emitted noise. Except for this, the experimental set up is identical to that shown in Figs. 1 and 8.

The variation of the output power with z as measured through our 1.5 GHz wide band pass filter is illustrated in Fig. 15. The power grows exponentially with a single

18

pass growth rate equal to 42 dB/m. Note that unlike the amplifier measurements of Fig. 14, saturation is not reached within the available length of our system. However, this is not surprising since the radiation must grow out of low level noise.

One obvious question is whether the superradiant emission is concentrated in the fundamental TE_{11} mode as was verified in our amplifier studies, or whether higher modes of the same frequency ω but different wave numbers k_z contribute to the output intensity. Therefore, as in the case of the amplifier (see Fig. 9) we made far field radiation measurements and the results are illustrated in Fig. 16(a). We now see, unlike Fig. 9, a large off-axis radiation lobe, suggesting higher mode excitation. A preliminary analytical examination indicates that the TM_{11} mode is a likely candidate. Its calculated radiation pattern is shown in Fig. 16(b) together with the pattern of the TE_{11} mode. Superpostion of the two may well lead to an overall pattern like that observed experimentally. However, at this time no detailed calculations of mode coupling are available.

Lastly it should be stressed that in order to insure single pass amplification in a high gain system like ours, the output window must have very low reflectivity. Otherwise multipass operation can occur, and eventually lead to parasitic system oscillations. We changed the window reflectivity from $R \simeq 2 \times 10^{-5}$ to $R = 10^{-1}$ and measured the power output as a function of interaction length. The measured small signal growth rate is now 91 dB/m, twice the value obtained with the better window (Fig. 15). This factor of two change is readily understood since the short voltage pulse length from the accelerator permits at most two amplifying passes through the CARM.

V. DISCUSSION

This paper reports details of the first[21,22] successful operation of a single pass cyclotron autoresonance maser amplifier. The observations are summarized in Table III. At a wavelength of 8.6 mm, power outputs of 12 MW have been achieved with an overall gain of approximately 30 dB. The corresponding electronic efficiency of converting electron beam energy to radiation is typically 6%. Waveguide attenuation (~ 0.6 dB/m) caused by the poor conductivity of stainless steel has somewhat degraded our system performance. Measured linear growth rates are ~ 55 dB/m. Excitation occures predominantly in the fundamental TE_{11} mode of the cicular waveguide. Good agreement with computer simulations has been achieved both in the linear and nonlinear regimes.

Measurements have also been carried out in the superradiant mode of operation wherein the high power magnetron driver is turned off and the radiation is allowed to grow out of spontaneously emitted noise. Power levels do not exceed ~ 100 kW and nonlinear saturation does not occur. Unlike in the amplifier case, multimoding (same ω, different $k_\perp$) now takes place. We thus conclude that multimoding can be suppressed by subjecting the CARM to a sufficiently large input signal.

As noted in the introduction, an undesirable downlifted mode having a frequency of 19.8 GHz could be excited to the detriment of the 35 GHz CARM. Under certain conditions this mode is absolutely unstable which leads to even more concern[23]. A numerical pinch point analysis delineating regions of absolute instability has been made

and the results are shown in Fig. 18. It can be seen that our CARM operates well outside regions where an absolute instability can be expected.

In our operating regime, the particle trajectory code predicts a non-negligible guiding center offset (see Fig. 7). This is clearly observed by the burn marks produced on the thermal paper placed in the path of the beam. The code also predicts a well defined coherent beam precession within the wiggler (with a spatial period of l_w). This has been confirmed experimentally as shown in Fig. 4(b). The code also predicts a coherent beam precession in the CARM region with a spatial period $\lambda_c = 2\pi v_x \gamma / \Omega_0$ (see Fig. 7). However, no such coherent precession is observed in the CARM region. This suggests that the electrons have been dispersed in their radial position as a result of passing across the rapidly varying wiggler field at the downstream wiggler terminus. This discrepancy with computer simulations is not understood. However, space charge effects, which are not included in the simulation may well be the culprit.

One may well ask whether our experiments shed light on the following question: Which of the two regimes $k_w v_z \gtrless \Omega_o / \gamma$ is preferable in spinning up the electron beam before injection into the CARM region? Unfortunately we have no simple, unequivocal answer. Insofar as the CARM characterisitics are concerned, there is little to choose between them.

REFERENCES

[1] N. S. Ginzburg, I. G. Zarnitsyna, and G. S. Nusinovich, *Radiophysics Quantum Electro.*, **24** , 331 (1981).

[2] J. L. Hirchfield, K. R. Chu, and S. Kainer, *Applied Phys. Letters*, **33**, 847 (1978).

[3] V. L. Bratman, N. S. Ginzburg, G. S. Nusinovich, M. I. Petelin, and P. S. Strelkov, *International J. Electronics*, **51**, 541 (1981).

[4] V. L. Bratman, G. G. Denisov, N. S. Ginzburg, and M. I. Petelin, *IEEE J. Quantum Electronics*, **QE-19**, 282 (1983).

[5] A. T. Lin, *Inter. Journal Electronics*, **57**, 1097 (1984).

[6] A. T. Lin and C. C. Lin, *Intern. J. Infrared and Millimeter Waves*, 6, 41 (1985).

[7] A. W. Fliflet, *Intern. Journal Electronics*, **61**, 1049 (1986).

[8] A. T. Lin and C. C. Lin, *Physics of Fluids*, **29**, 1348 (1986); also K. R. Chu and A. T. Lin, *IEEE Trans. Plasma Science*, **16**, 90 (1988).

[9] C. Chen and J. S. Wurtele, (submitted for publication, 1990).

[10] A. T. Lin, K. R. Chu, and A. Bromborsky, *IEEE Trans. Electron Devices*, **ED-34**, 2621 (1987).

[11] B. G. Danly, K. D. Pendergast, R. J. Temkin and J. A. Davies, *Proc. Soc. Photo-Opt. Instrum Eng.*, **873**, 143 (1988); K. D. Pendergast, B. G. Danly, R. J. Temkin and J. S. Wurtele , *IEEE Trans. Plasma Science*, **16**, 122 (1988); C. Chen and J. S. Wurtele, *Phys. Rev.*, **A40**, 489 (1989).

[12] J. K. Lee, W. D. Bard, S. C. Chiu, R. C. Davidson, and R. R. Goforth, *Physics of Fluids*, **31**, 1824 (1988).

[13] B. G. Danly, K. D. Pendergast, and R. J. Temkin, *13th Inter. Conf. on Infrared and Millimteter Waves*, Honolulu HI, December, 1988.

[14] B. G. Danly, J. A. Davies, K. D. Pendergast, R. J. Temkin and J. S. Wurtele, *Proc. SPIE*, **1061**, 243 (1989).

[15] R. B. McCowan, A. W. Fliflet, S. H. Gold, W. M. Black, A. K. Kinkead, V. L. Granatstein and M. Sucy, *IEEE Trans. Electron Devices*, **36**, 1968 (1989).

[16] Q. S. Wang, A. T. Lin, N. C. Luhmann and D. B. McDermott, *Bull. Am. Phys. Soc.*, **34**, 2089 (1989).

[17] M. Caplan, B. Kulke, G. Westenskow, D. B. McDermott, and N. C. Luhmann, *12th Inter. Conf. Free Electron Lasers*, Paris, France, 1990, page 76.

[18] I. E. Botvinnik, V. L. Bratman, A. B. Volkov, N. S. Ginzburg, C. G. Denisov, B. D. Kol'chugin, M. M. Ofitserov, and M. I. Petelin, *Pis'ma Zh. Eksp. Teor. Fiz.*, **35**, 418 (1982).

[19] I. E. Botvinnik, V. L. Bratman, A. B. Volkov, G. G. Denisov, B. D. Kol'chugin, and M. M. Ofitserov, *Pis'ma Zh. Eksp. Teor. Fiz.*, **8**, 1376 (1982); also *Soviet Tech Phys. Letters*, **8**, 596 (1982).

[20] R. M. Gilgenbach, J. G. Wang, J. J. Choi, C. A. Quitten and T. A. Spencer, *Bull. Am. Phys. Soc.*, **34**, 2088 (1989); also *11th Inter. Conf. on FEL Conference Digest*, Naples, Florida, 1989, page 54.

[21] G. Bekefi, A. C. DiRienzo, C. Leibovitch and B. G. Danly, *Appl. Phys. Letters*, **54**, 1302 (1989).

[22] A. C. DiRienzo and G. Bekefi, *SPIE International Soc. Optical Engineering*, **1226**, 209 (1990).

[23] J. A. Davies, *Phys. Fluids*, **B1**, 663 (1989); also J. A. Davies, R. C. Davidson and G. L. Johnston, *IEEE Trans. Plasma Science*, **18**, 286 (1990).

[24] D. B. Hopkins and G. T. Konrad, Lawrence Berkeley Laboratory, Collider Physics Group, Report No. CP-49, (1989).

[25] R. H. Jackson, S. H. Gold, R. K. Parker, H. P. Freund, P. C. Efthimion, V. L. Granatstein, M. Herndon, A. K. Kinkead, J. E. Kosakowski, and T. J. Kwan, *IEEE J. Quant. Electron.*, **QE-19**, 346 (1983).

[26] T. J. Orzechowski and G. Bekefi, *Phys. Fluids*, **19**, 43 (1976).

[27] The technique is described by D. Prosnitz and E. T. Scharlemann, Lawrence Livermore National Laboratory, ATA Note No. 229, Feb. 22, 1984.

[28] J. Fajans, *J. Appl. Phys.*, **55**, 43 (1984).

[29] J. Fajans, G. Bekefi, Y. Z. Yiu and B. Lax , *Phys. Fluids*, **28**, 1995 (1985).

[30] L. Friedland, *Phys. Fluids*, **23**, 2376 (1980).

[31] A. K. Ganguly, and H. P. Freund, *Phys. Rev.*, **A32** 2275 (1985); also *IEEE Trans. Plasma Science*, **16**, 167 (1988).

[32] K. D. Pendergast (private communication).

[33] A. C. DiRienzo, Ph. D. Thesis, Dept. of Physics, Massachusetts Institute of Technology, Cambridge, MA, (1990), (unpublished).

[34] M. N. Afsar, *IEEE Trans. Misrowave Theory, Technique*, **32**, 1598 (1984).

[35] A. C. Ludwig, *IEEE Trans. Antenna and Propagation* , **14**, 434 (1966). The phase variation over the tranmitting antenna aperture has been incorporated in the calculations of the radiation field patterns.

TABLE I   **Electron Beam Characteristics**

| Parameter | Beam Radius r_b | |
	0.076 cm	0.318 cm
Current I_b (A)	5.0	195
Normalized Brightness B_n (Acm^{-2}rad^{-2})	3.2×10^4	5×10^3
Normalized Emittance ϵ_n (cm - rad)	5.9×10^{-3}	9.4×10^{-2}
$\Delta p_z / m_0 c$	1.6×10^{-3}	2.4×10^{-2}
$\Delta \gamma_z / \gamma_z$	0.003	0.044

TABLE II   **Magnetic Wiggler Characteristics**

Wiggler Type	Group I	Group II
Wiggler period (cm)	4.06	7.00
Wiggler length (cm)	27	44
Field strength B_w (G)	840	490
Mean $\langle \alpha \rangle = \langle \beta_\perp / \beta_z \rangle$ (calculated)	0.27	0.30

TABLE III   CARM Characteristics

Wiggler Type	Group I	Group II
Beam Energy (γ)	3.94	3.94
Beam Current (A)	128	128
Axial magnetic field B_z (kG)	5.4	6.1
Rf frequency (GHz)	34.73	34.73
Rf input power (kW)	17	18
Rf output power (MW)	12.2	8.7
Saturated efficiency (%)	6.3	4.5
Linear growth rate (dB/m)	50	62

FIGURE CAPTIONS

Figure 1: Experimental arrangement showing (a) the overall system, and (b) details of the electron gun.

Figure 2: Oscilloscope traces of the voltage, beam current and radiation intensity. (The voltage trace is corrected for inductive effects.)

Figure 3: Electron beam current leaving the emittance selector as a function of (a) the axial magnetic field, and (b) the square of the axial magnetic field. In the latter case, the linear relationship indicates constant beam brightness (see text).

Figure 4: Wiggler field characterisitics; (a) measurements of the wiggler field strength as a function of axial position, and (b) marks left on an axially movable witness plate within the wiggler, showing coherent beam precession. The central spot is for the case when the wiggler field is turned off.

Figure 5: Normalized axial electron velocity as a function of the applied axial magnetic field for electrons executing ideal orbits. The upper curve is for the short period wiggler (type I orbits), and the lower curve is for the long period wiggler (type II orbits). The dashed lines illustrate the operating field strength [see Table II].

Figure 6: Particle code calculations of (a) the average tranverse beam velocity and (b) the average energy spread as a function of axial position for the type I wiggler. ($B_z = 5.4$ kG, $B_w = 840$ G)

Figure 7: Particle code calculations of the transverse electron beam profile for three successive axial positions in the CARM region separated

by a third of a cyclotron period; r_L denotes the offset of the beam guiding center, and r_L the average electron Larmor radius ($B_z = 5.4$ kG, $B_w = 840$ G).

Figure 8: The 35 GHz wave system showing (a) the overall view, (b) details of the wave launcher, and (c) details of the wave transmitter.

Figure 9: The measured far field radiation pattern for (a) the magnetron alone and (b) for the operating CARM amplifier. The calculated radiation pattern takes proper account of the tranverse phase variation of the wave over the face of the transmitting horn.

Figure 10: Geometry of an electron orbit used in the CARM simulations.

Figure 11: Radiation intensity as a function of axial position in the CARM, showing a comparison of linear theory (dashed line) with nonlinear computer simulation (solid line). [V = 1.5 MeV; I = 128A; $\Delta\gamma_z/\gamma_z = 0$; $B_z = 5.62$ kG; $\alpha = 0.27$; frequency = 34.7 GHz]

Figure 12: Computer simulations of the CARM amplifier; (a) linear growth rate and saturated efficiency as a function of energy spread, and (b) saturated power output as a function of frequency [$\gamma = 4.0$, I = 128A, $B_z = 5.4$ kG, $\alpha = 0.27$; in (a), $\omega/2\pi = 34.7$ GHz; in (b), $\Delta\gamma_z/\gamma_z = 0.044$].

Figure 13: Radiation intensity (a) as a function of axial magnetic field at constant wiggler field; and (b) as a function of wiggler field at constant axial field [Type II wiggler; $\gamma = 3.94$, I = 128A].

Figure 14: Comparison of the measured and computed RF output power as a function of length of the CARM interaction region for (a) the

type I wiggler and (b) the type II wiggler [parameters are listed in Tables I, II and III].

Figure 15:   Measured RF output power as a function of interaction length under superradiant operation; [output window reflectivity $= 2 \times 10^{-5}$].

Figure 16:   Far-field radiation patterns; (a) measured under superradiant operation, showing multimoding; (b) computed patterns for the TE_{11} and TM_{11} waveguide modes.

Figure 17:   Normalized radiation intensity as a function of interaction length under superradiant operation. [Output window reflectivity $= 0.1$]

Figure 18:   Electron current as a function of $\alpha \equiv \beta_\perp / \beta_z$, delineating the region of absolute instability of the downshifted (gyrotron) mode for the parameters of this experiment.

WAVE LAUNCHER BIFILAR HELICAL WIGGLER CYLINDRICAL DRIFT TUBE

TO MARX ACCELERATOR

CARM INTERACTION REGION

FIELD EMISSION CATHODE

ANODE AND EMITTANCE SELECTOR

SOLENOID

(a)

VOLTAGE MONITOR ROGOWSKI

ROGOWSKI

GRAPHITE ANODE
.636 cm

GRAPHITE CATHODE

1.78 cm

1 cm gap

2.6 cm

17.2 cm
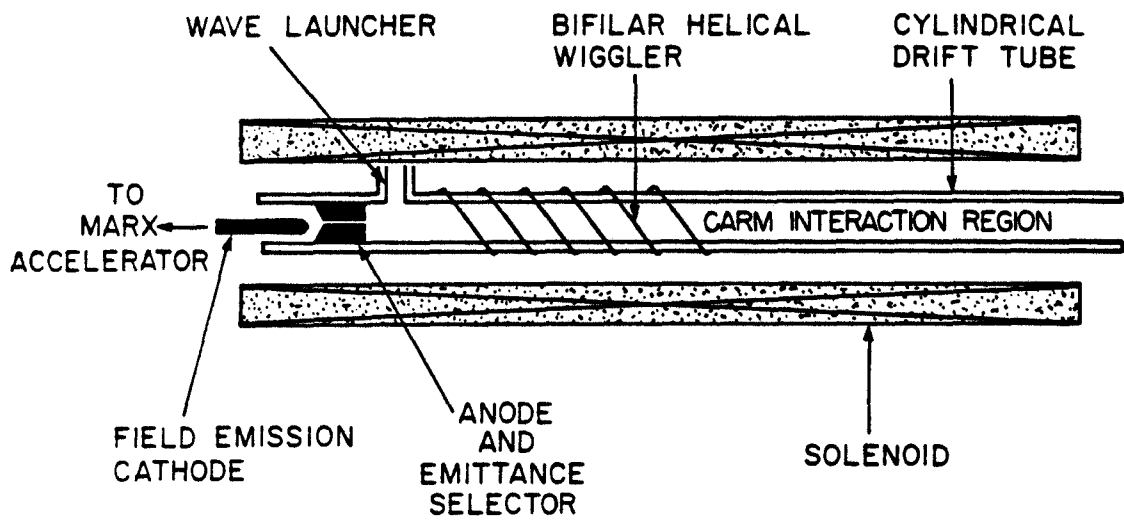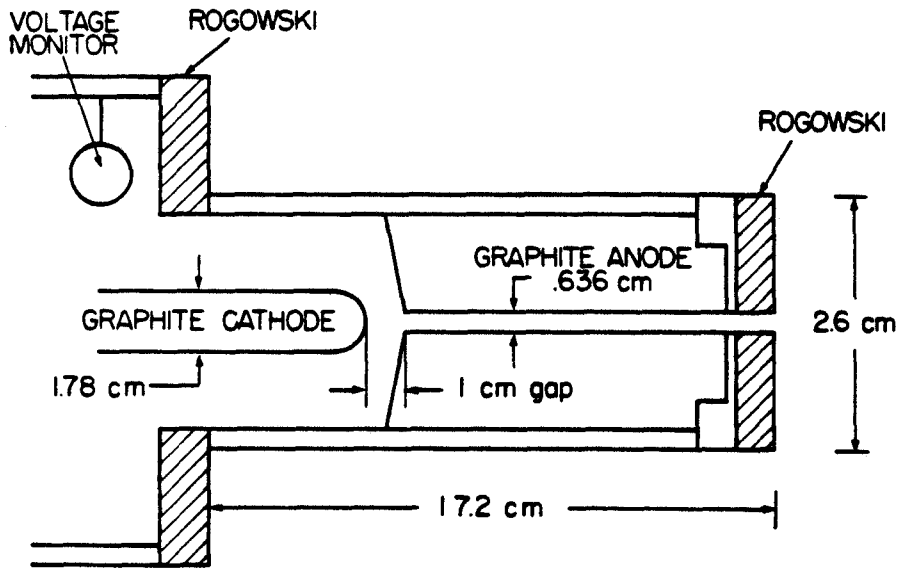
(b)
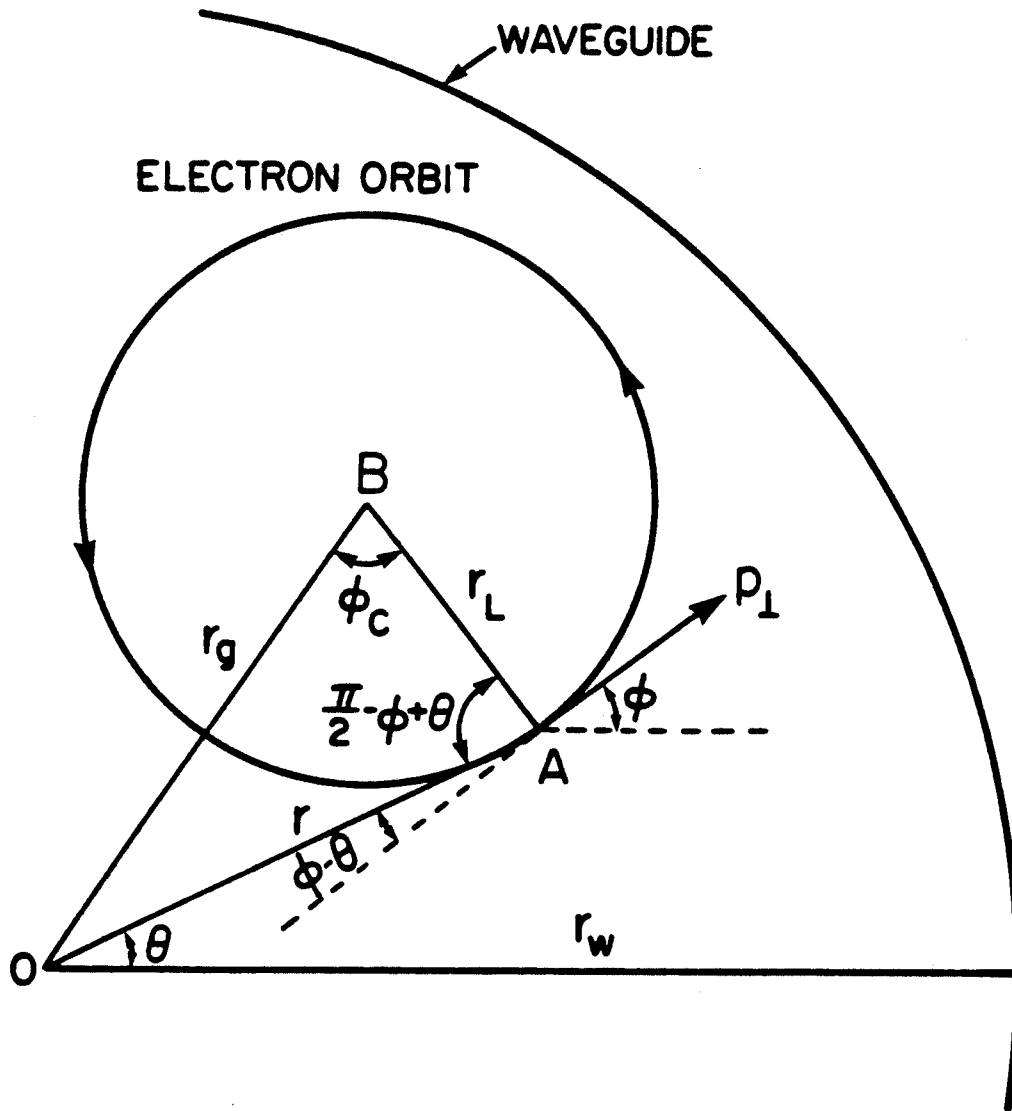
Fig.1. DiRienzo,Bekefi,Chen
Wurtele
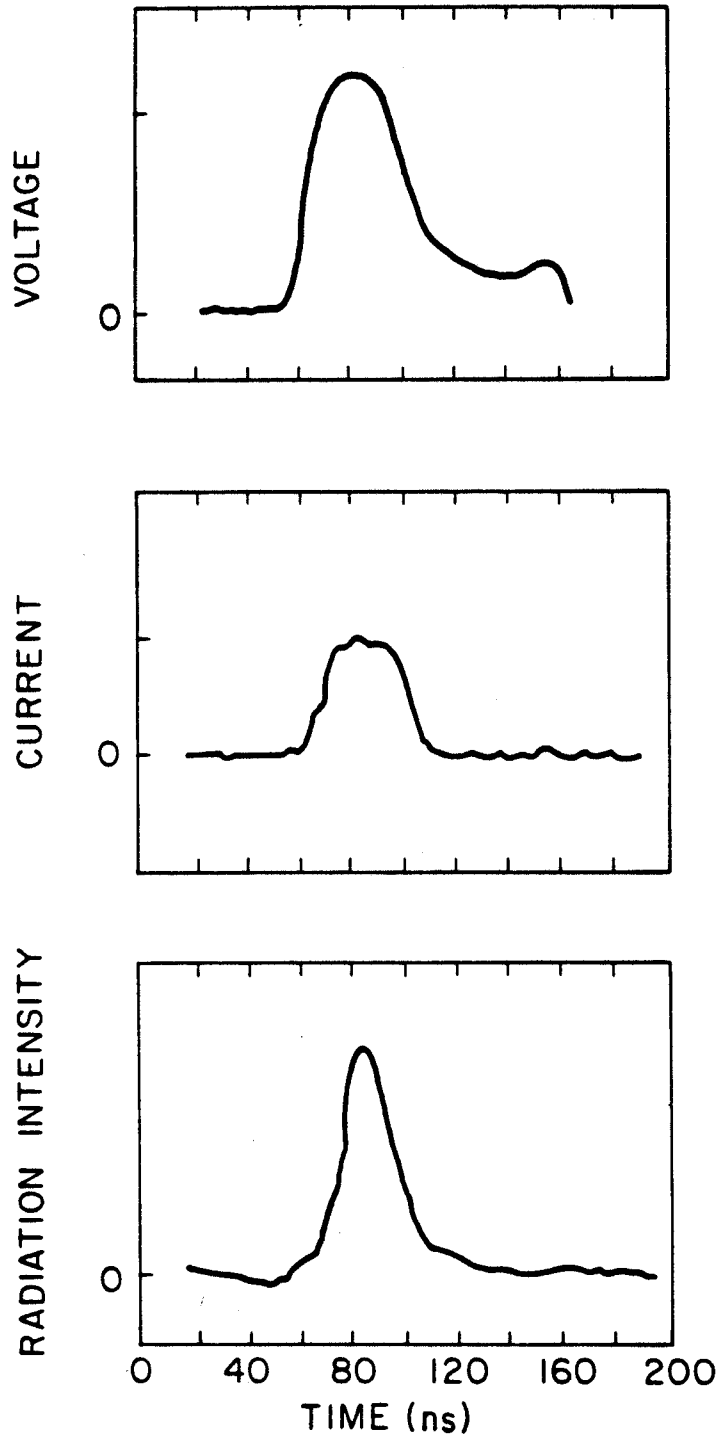
Fig.2. DiRienzo,Bekefi,Chen,
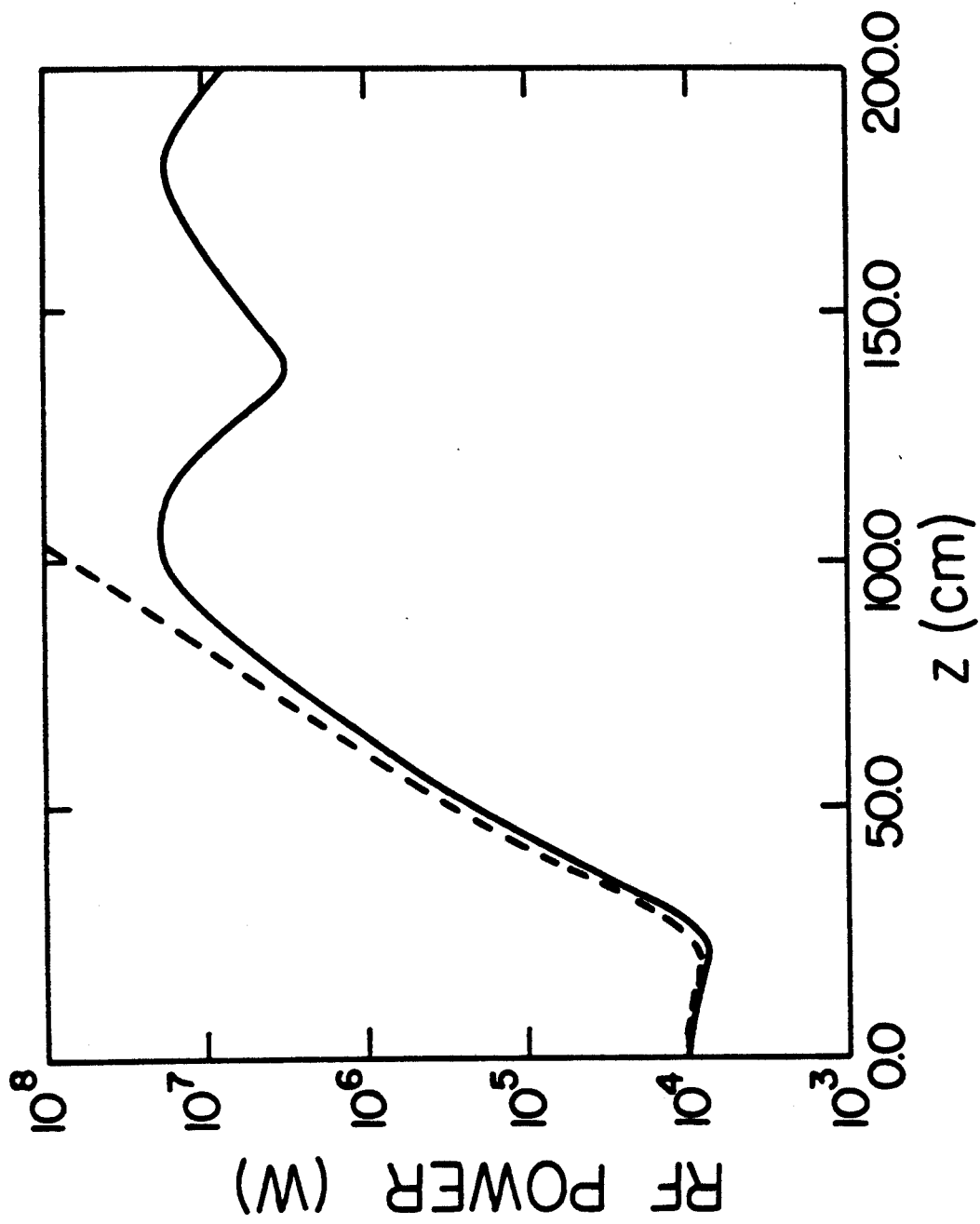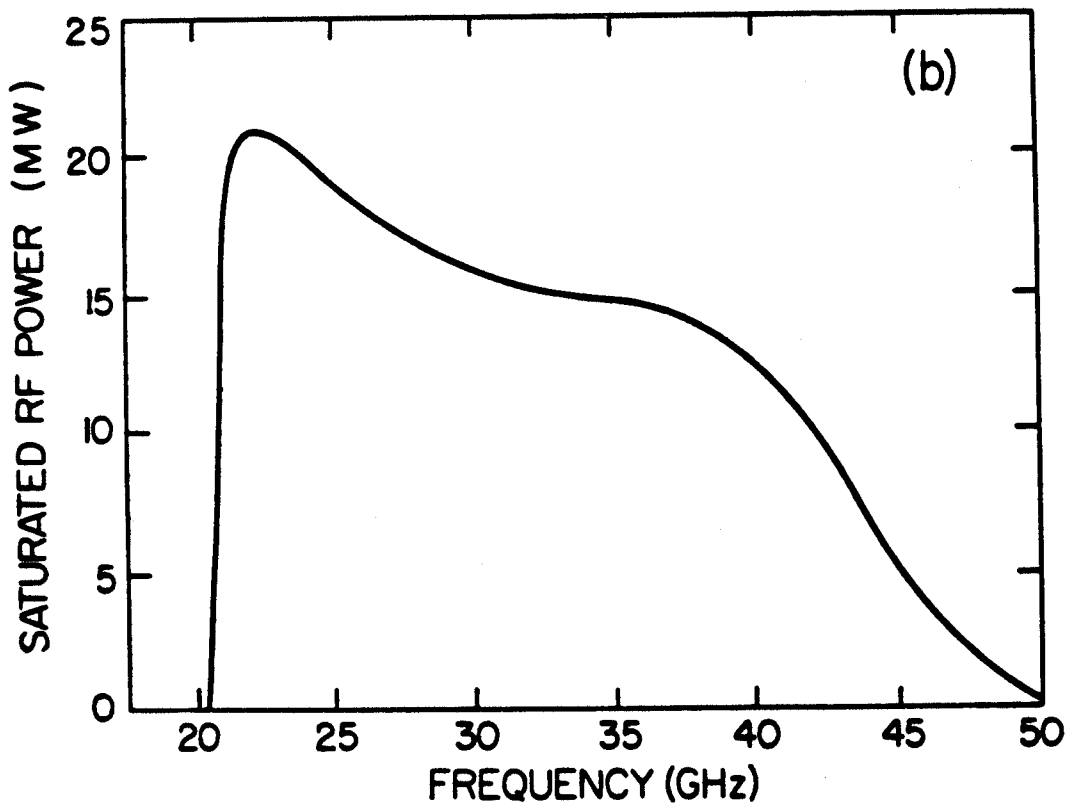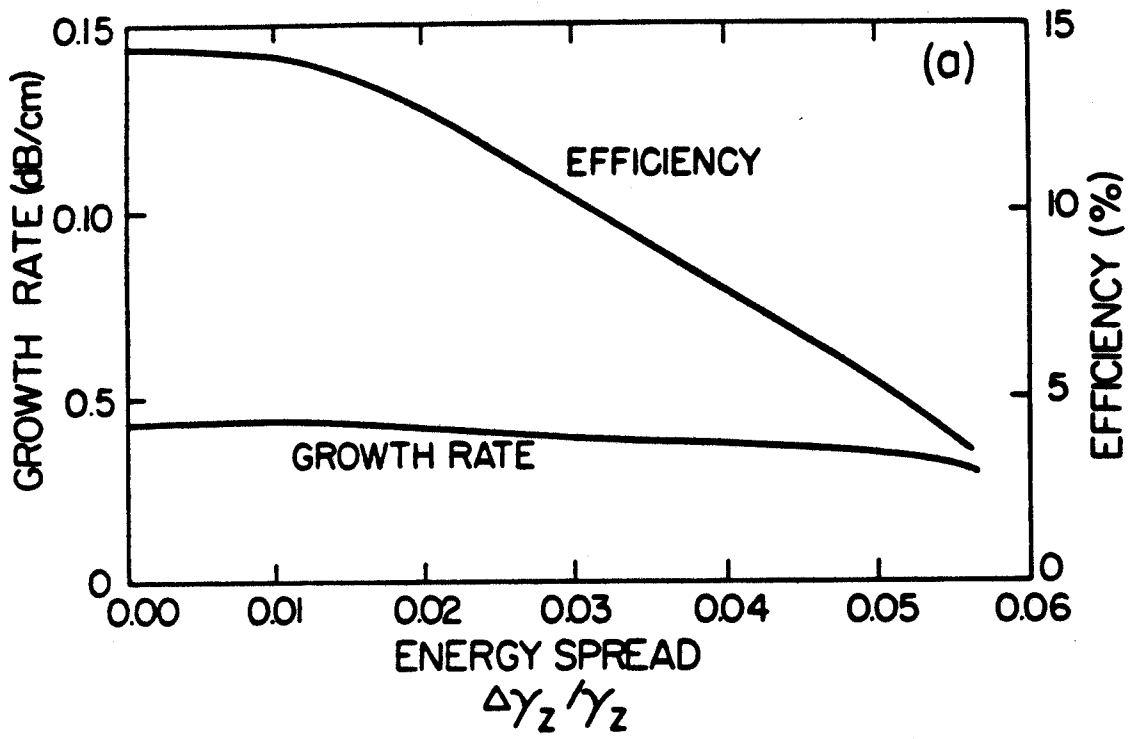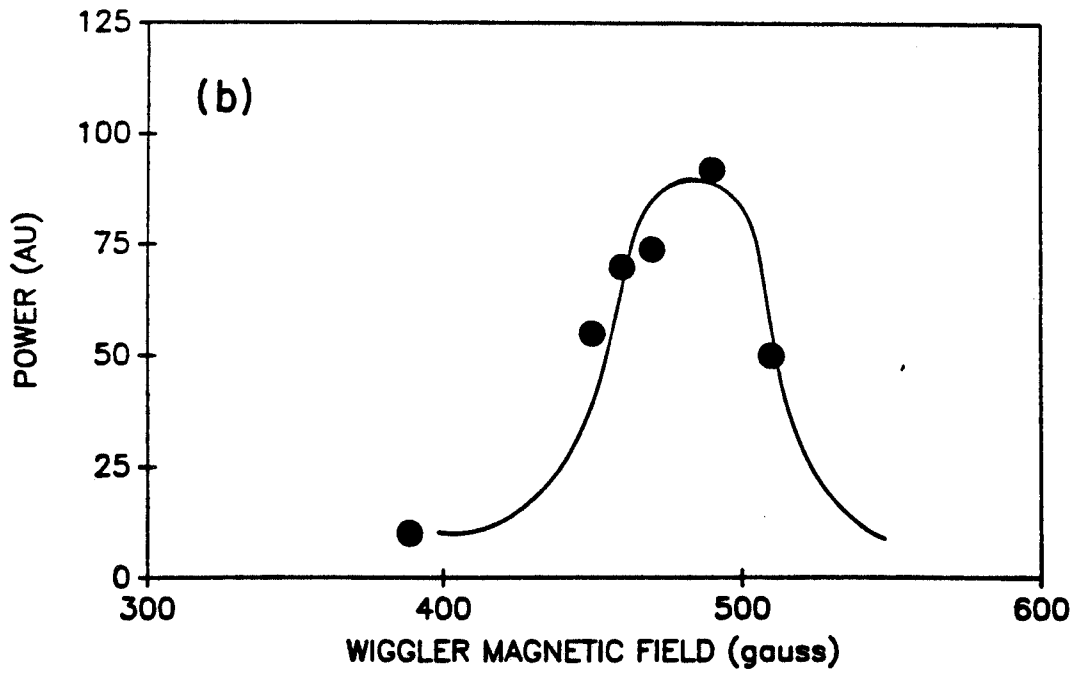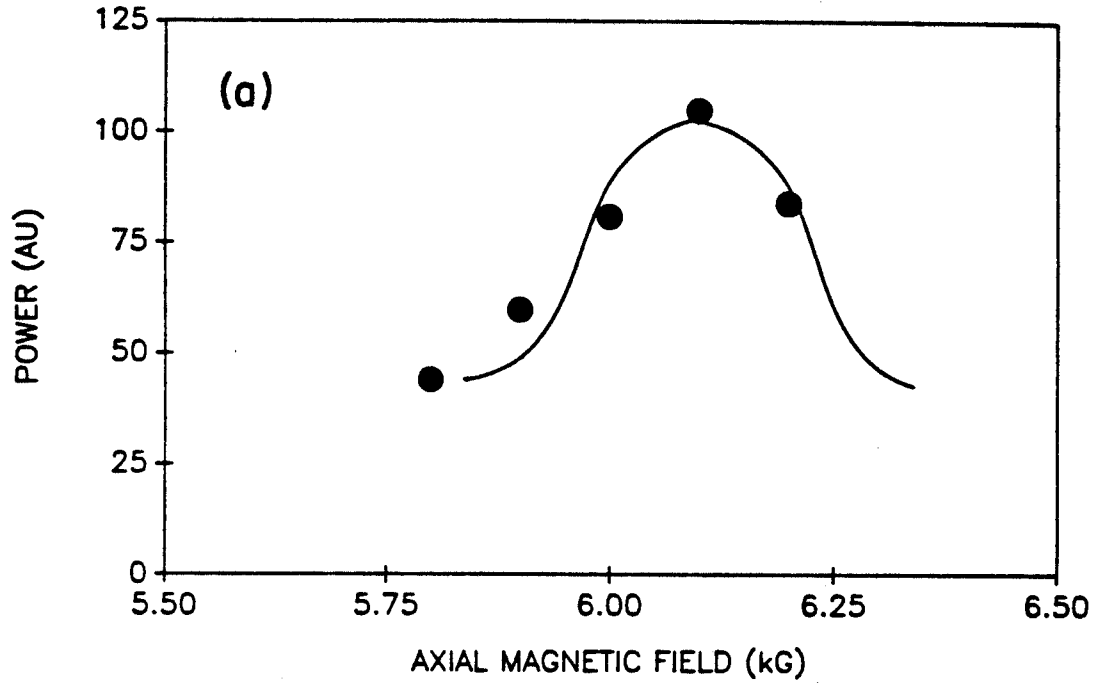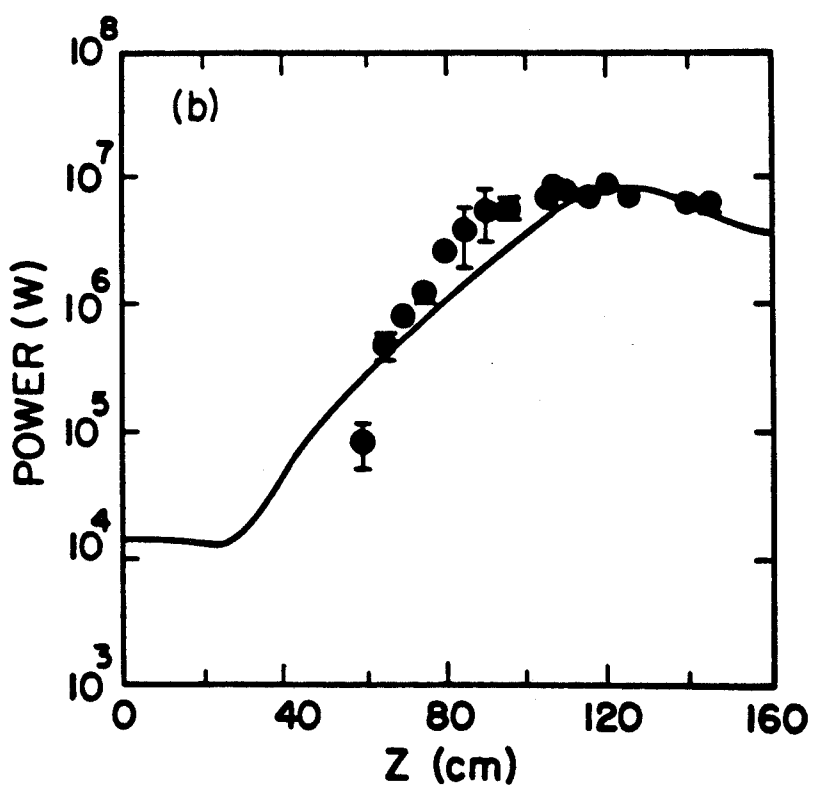Wurtele

32
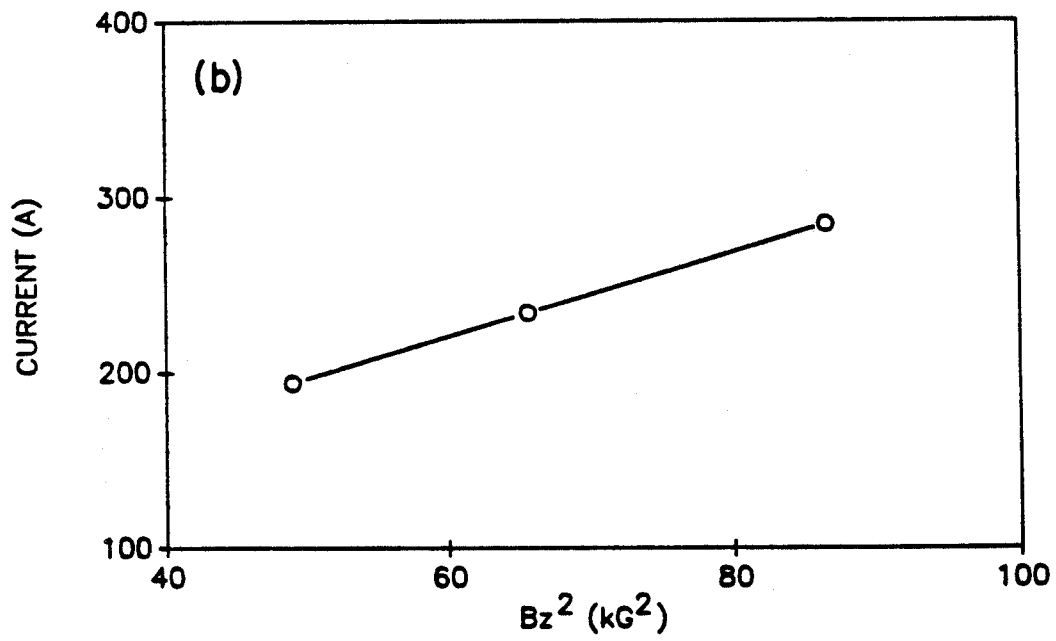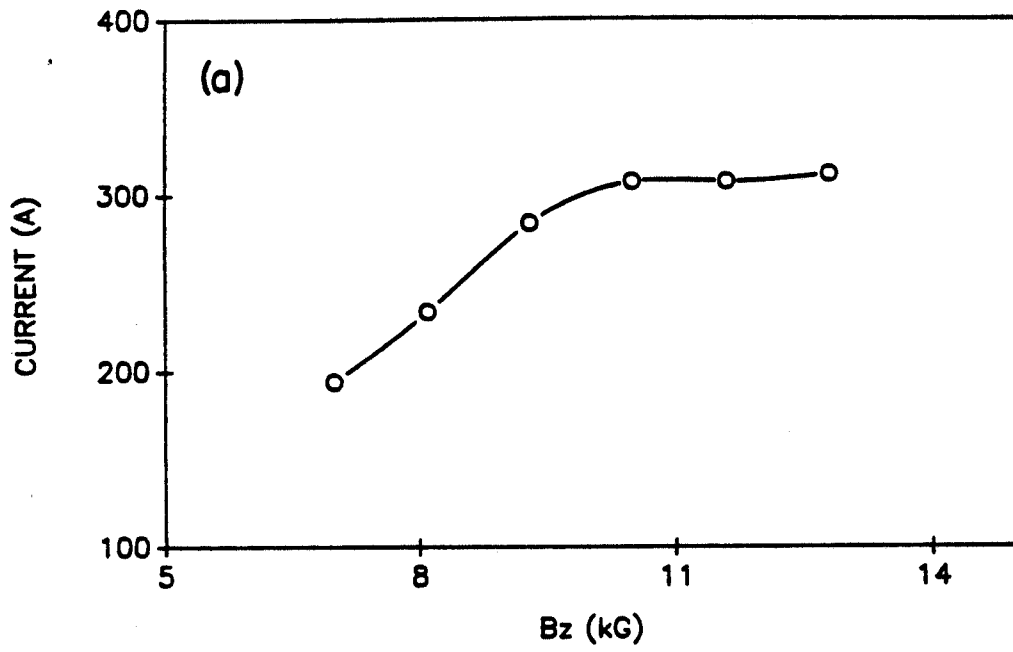
Fig.3. DiRienzo,Bekefi,Chen,
        Wurtele

33

(a)

(b)
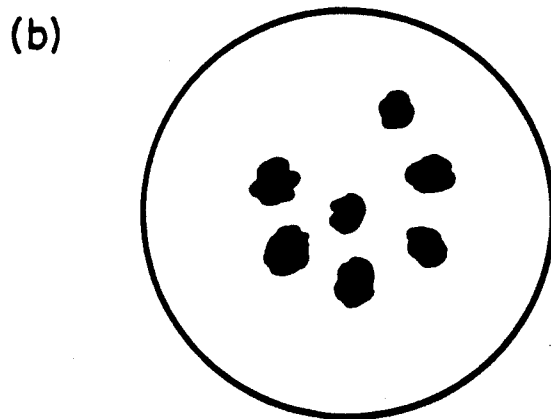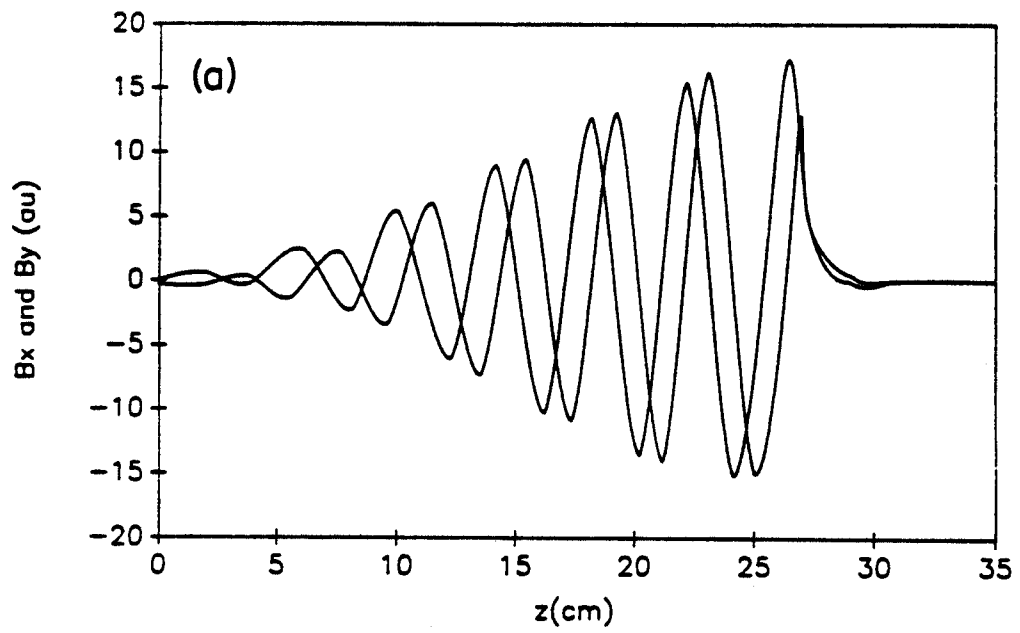
Fig.4. DiRienzo,Bekefi,Chen,
Wurtele

34

Fig.5. DiRienzo,Bekefi,Chen,
Wurtele

35

$\dfrac{\beta_\perp}{\beta_z}$

WIGGLER TERMINATION

(a)

z (m)

$\dfrac{\Delta \gamma_z}{\gamma_z}$

WIGGLER TERMINATION

(b)

z (m)

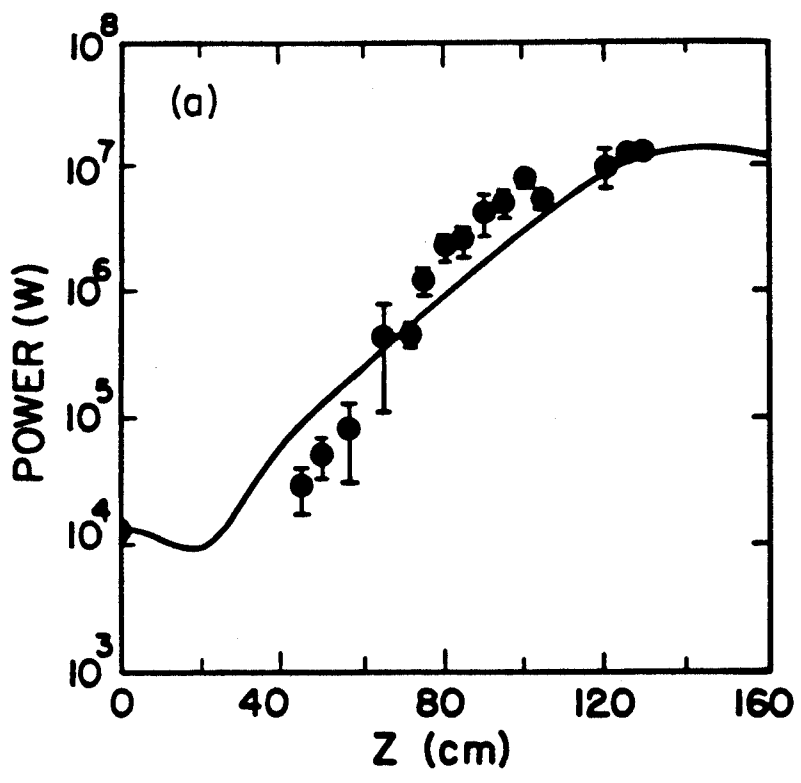Fig.6. DiRienzo,Bekefi,Chen,
Wurtele

36

Fig.7. DiRienzo,Bekefi.Chen,
Wurtele

CRYSTAL DETECTOR

BAND PASS FILTER (35±1)GHz

VARIABLE ATTENUATOR

SOLENOID

ANECHOIC CHAMBER

WIGGLER

CARM

CATHODE

ANODE

WAVE LAUNCHER

35 GHz MAGNETRON

(a)

0.71 cm

Ka BAND WAVEGUIDE

e-BEAM

1.587 cm

0.635 cm

WIGGLER

10.16 cm

6.35 cm

(b)

0.59 cm

6.6 cm

TPX

PLASTIC WINDOW

1.59 cm

10 cm
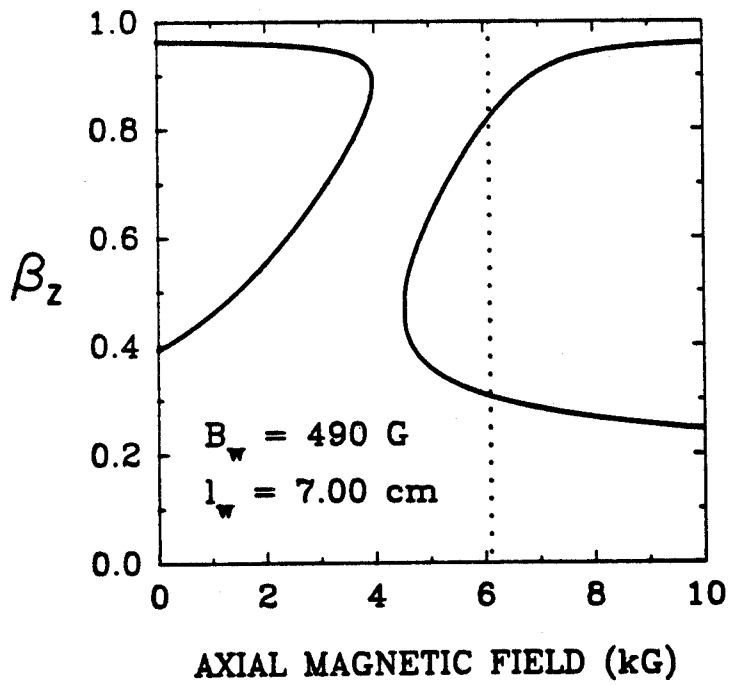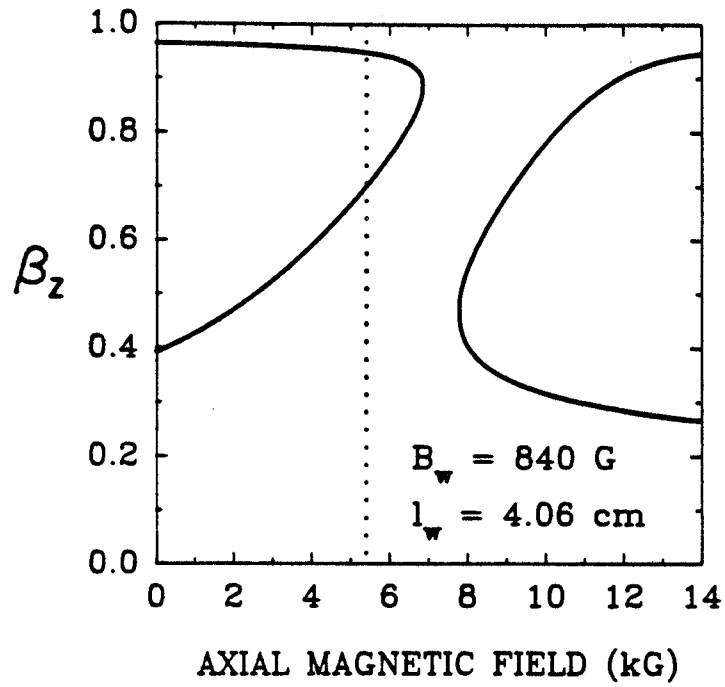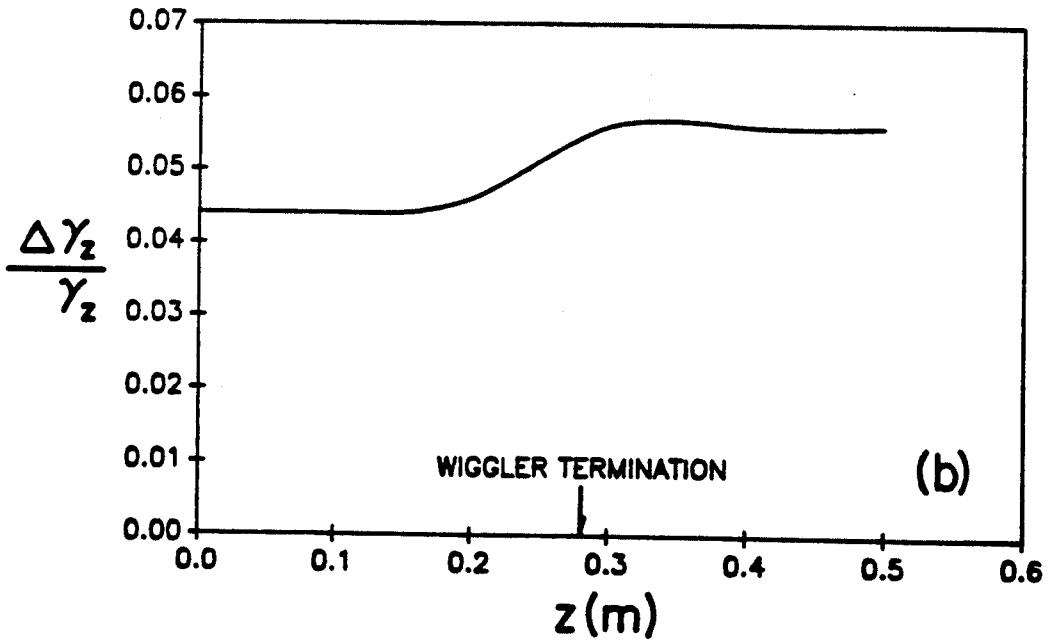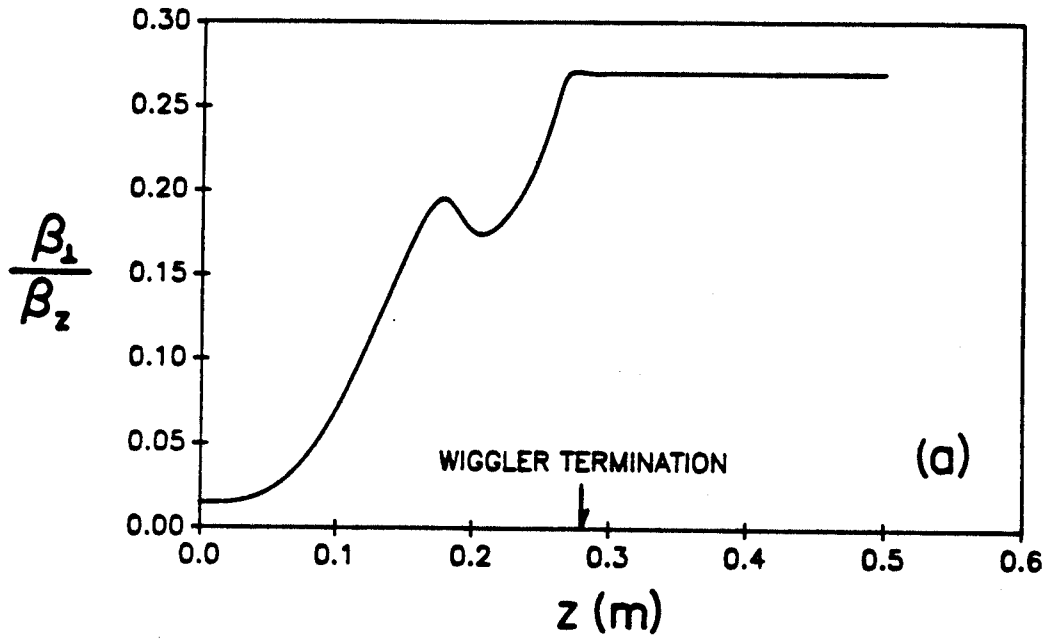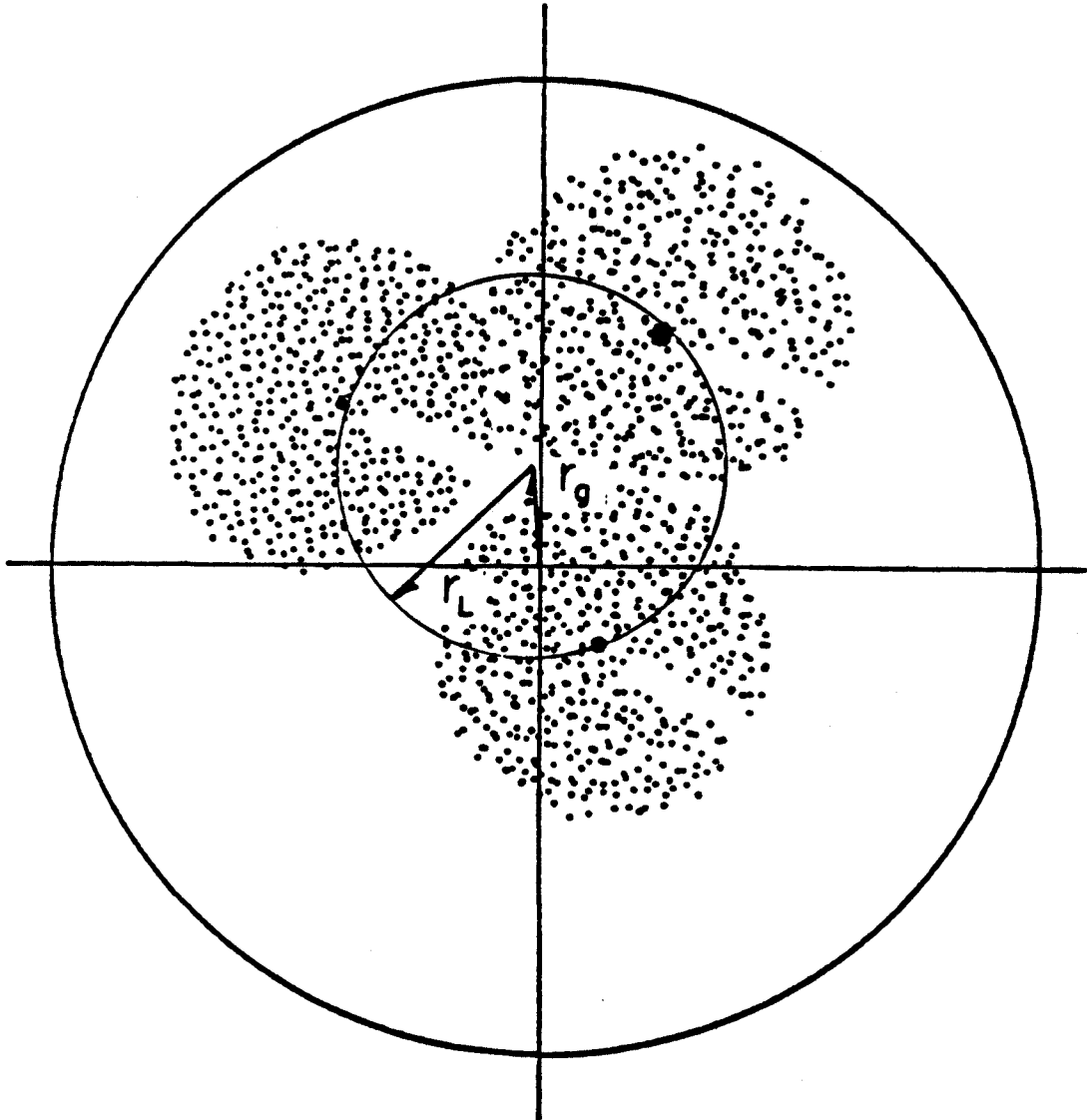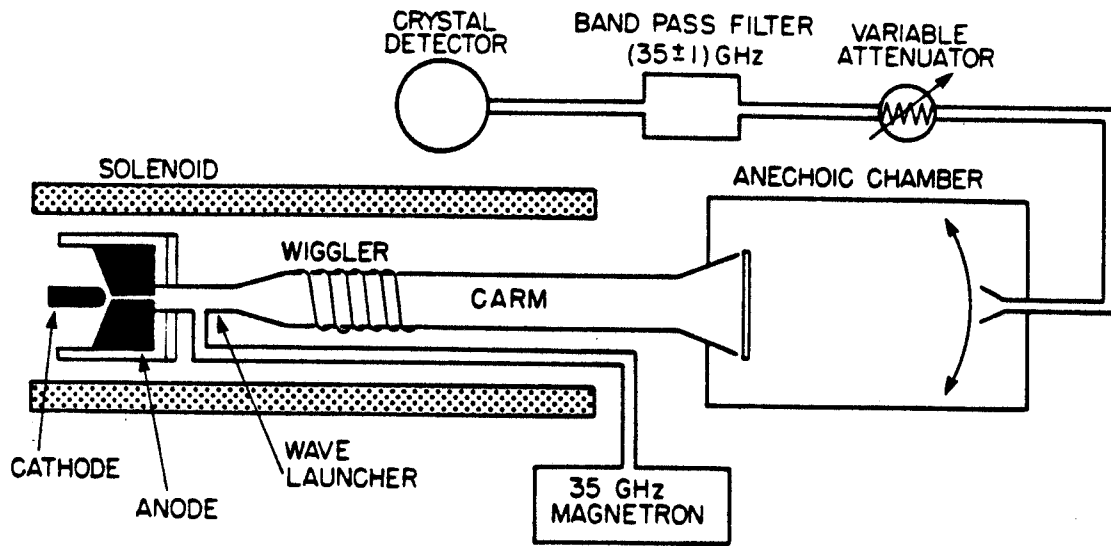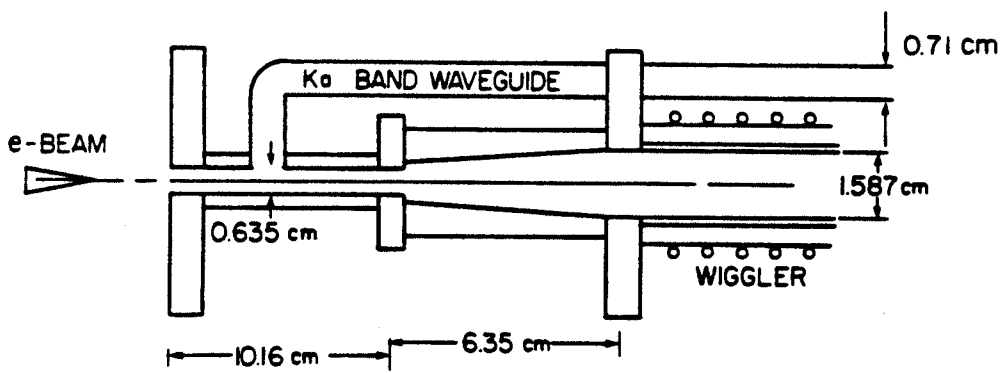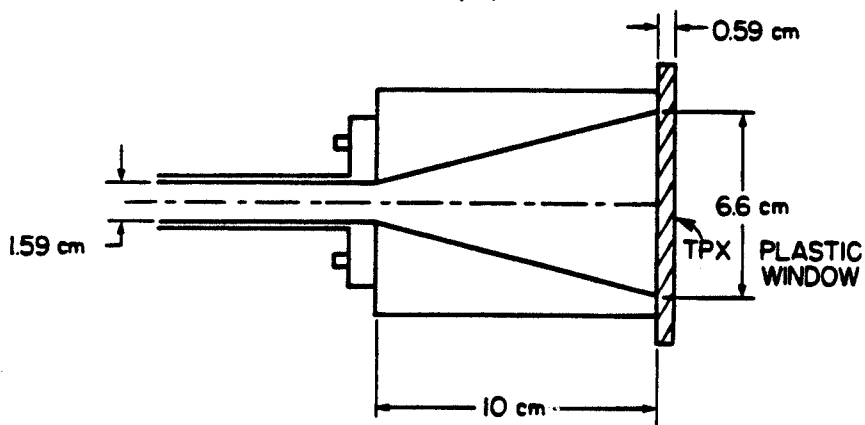
(c)

Fig.8. DiRienzo,Bekefi,Chen, Wurtele
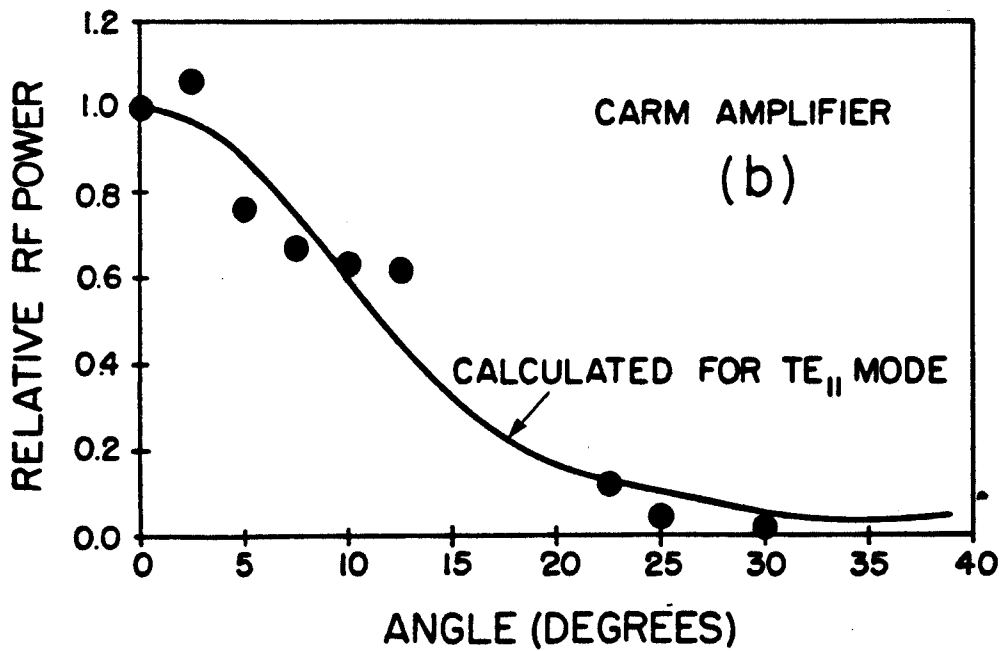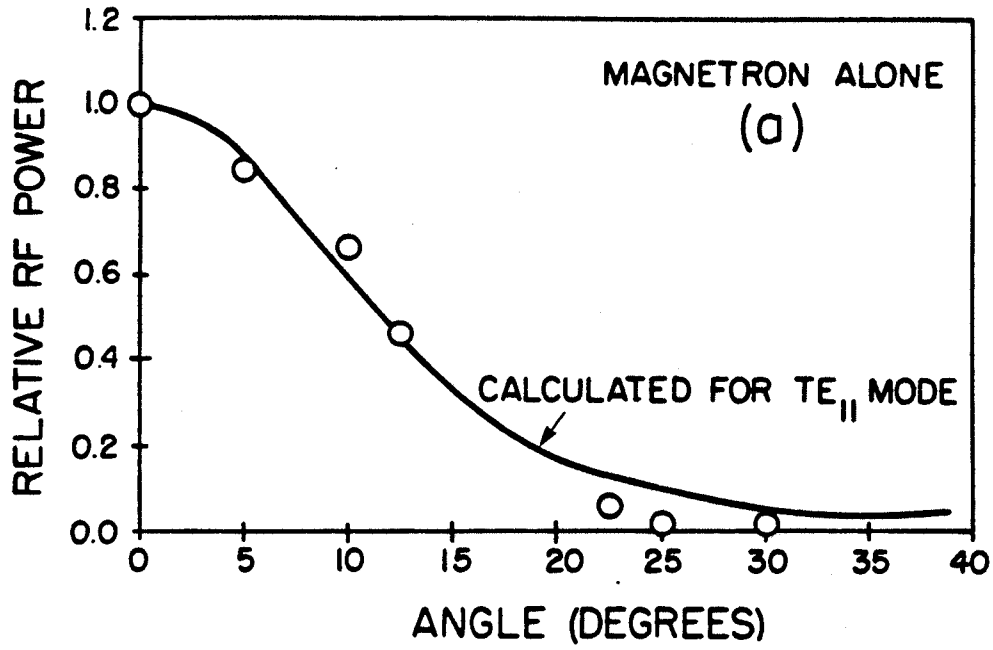
Fig.9 DiRienzo,Bekefi,Chen,
Wurtele

39

WAVEGUIDE

ELECTRON ORBIT

ϕ_c

r_L

r_g

$\frac{\pi}{2} - \phi + \theta$

B

A

$p_\perp$

ϕ

r

$\phi - \theta$

O

θ

r_w

Fig.10. DiRienzo,Bekefi,Chen, Wurtele

40

Fig.11. DiRienzo,Bekefi,Cl Wurtele

41

Fig.12. DiRienzo,Bekefi,Chen,
Wurtele

Fig.13 DiRienzo,Bekefi,Chen,
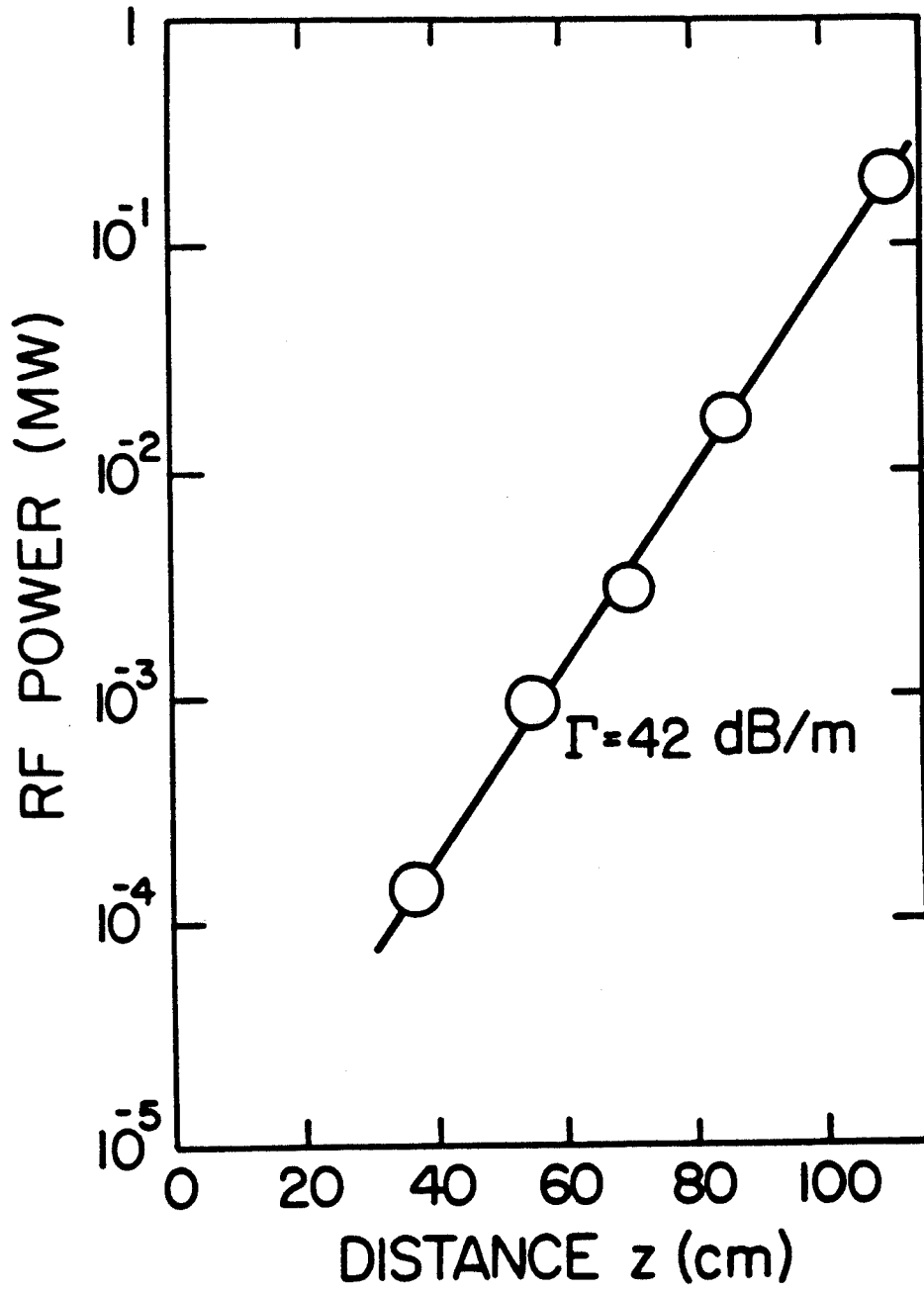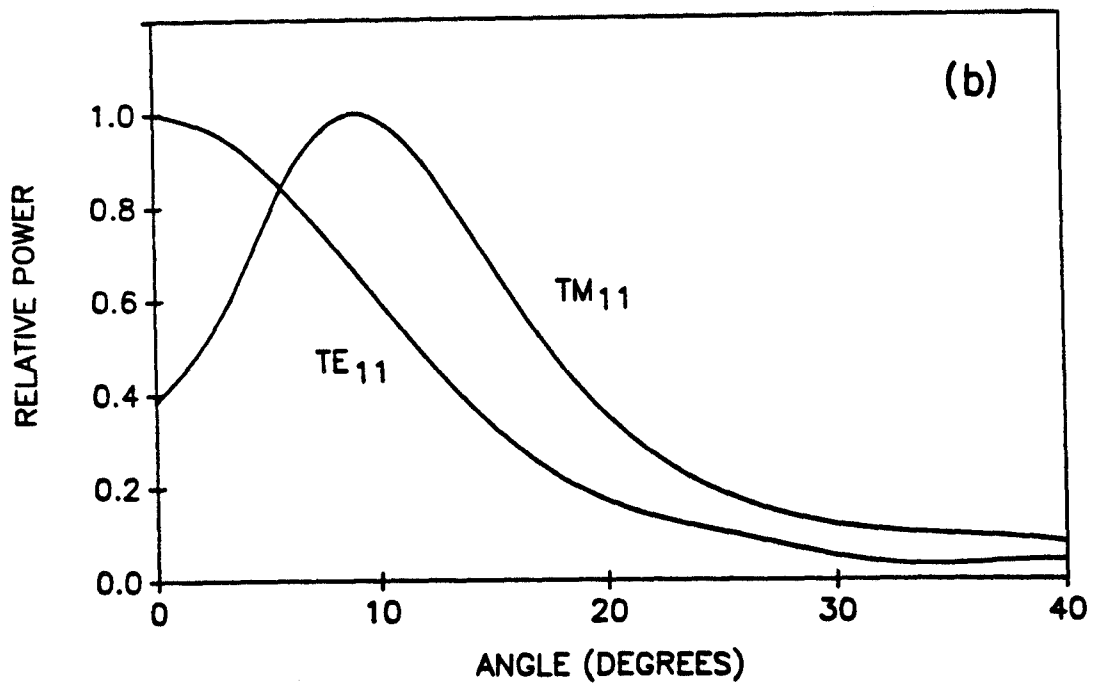   Wurtele

43

Fig.14. DiRienzo,Bekefi,Chen,
Wurtele

44

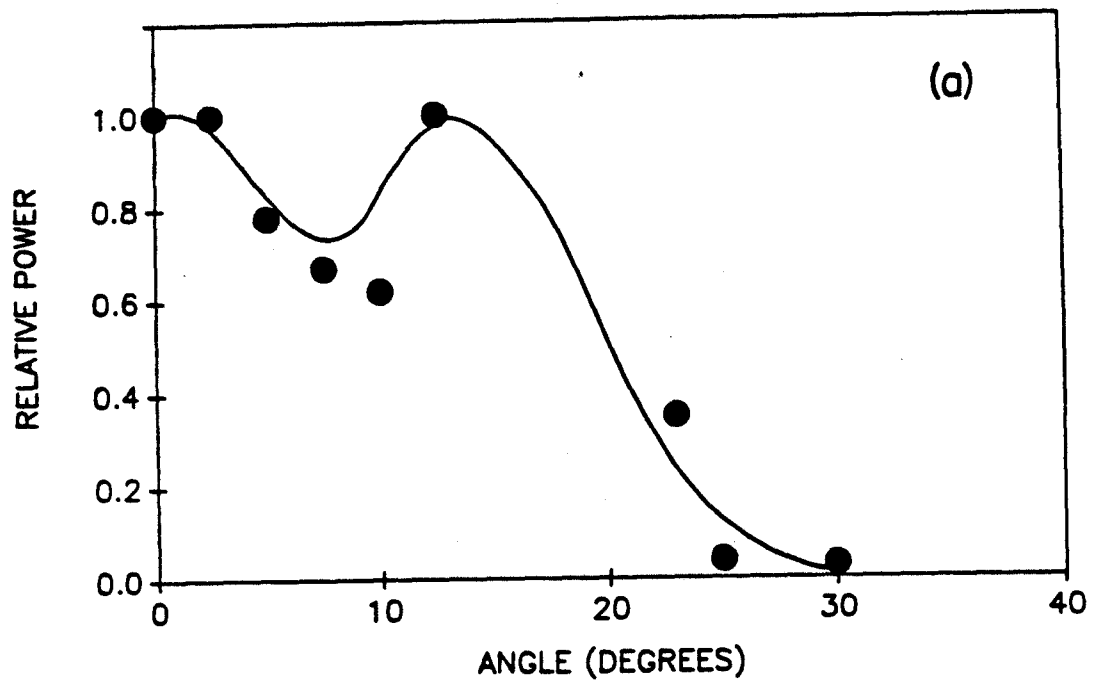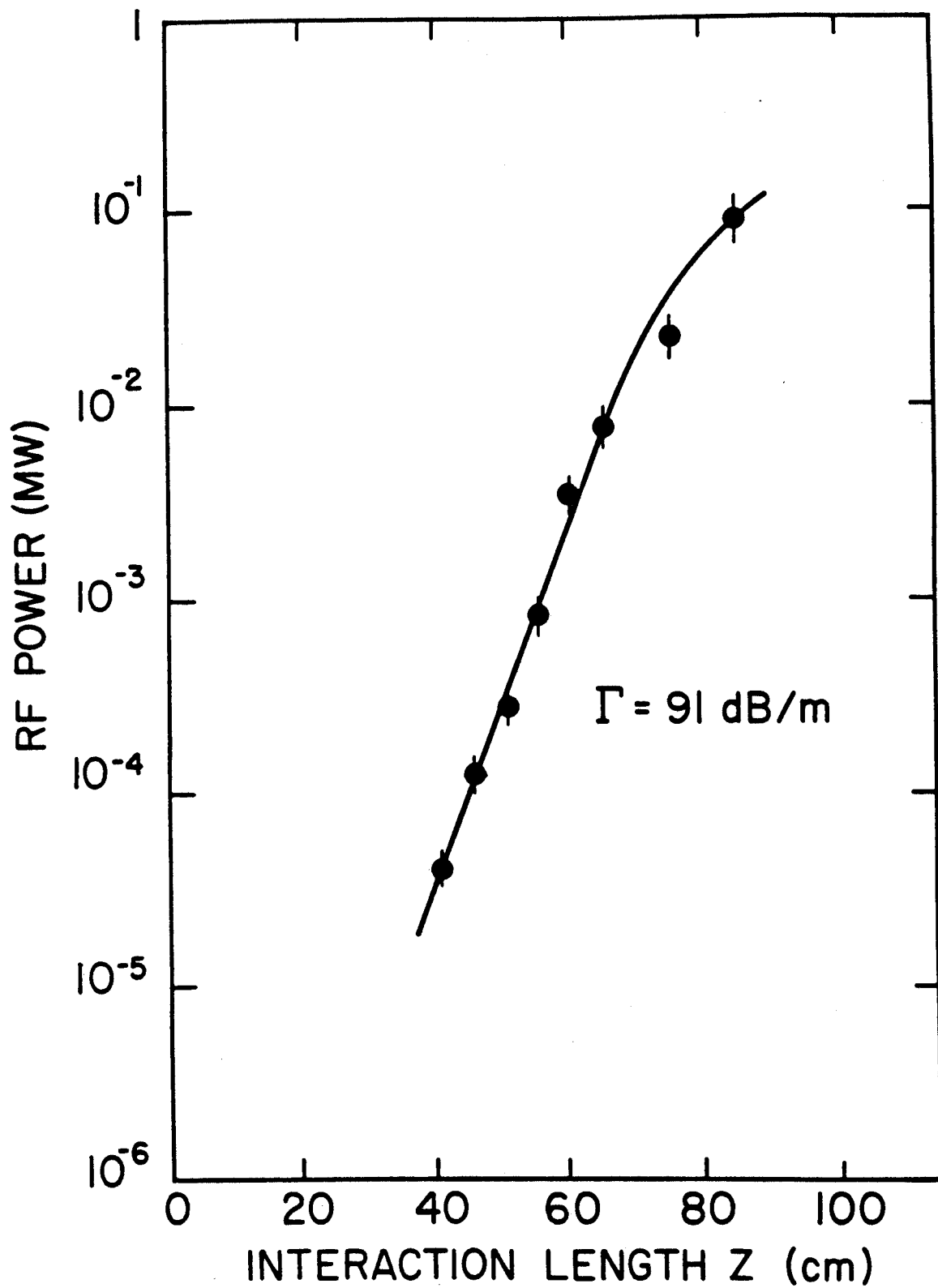Fig.15. DiRienzo,Bekefi,Chen,
Wurtele

45

(a)

RELATIVE POWER

ANGLE (DEGREES)

(b)

RELATIVE POWER

TM$_{11}$

TE$_{11}$

ANGLE (DEGREES)
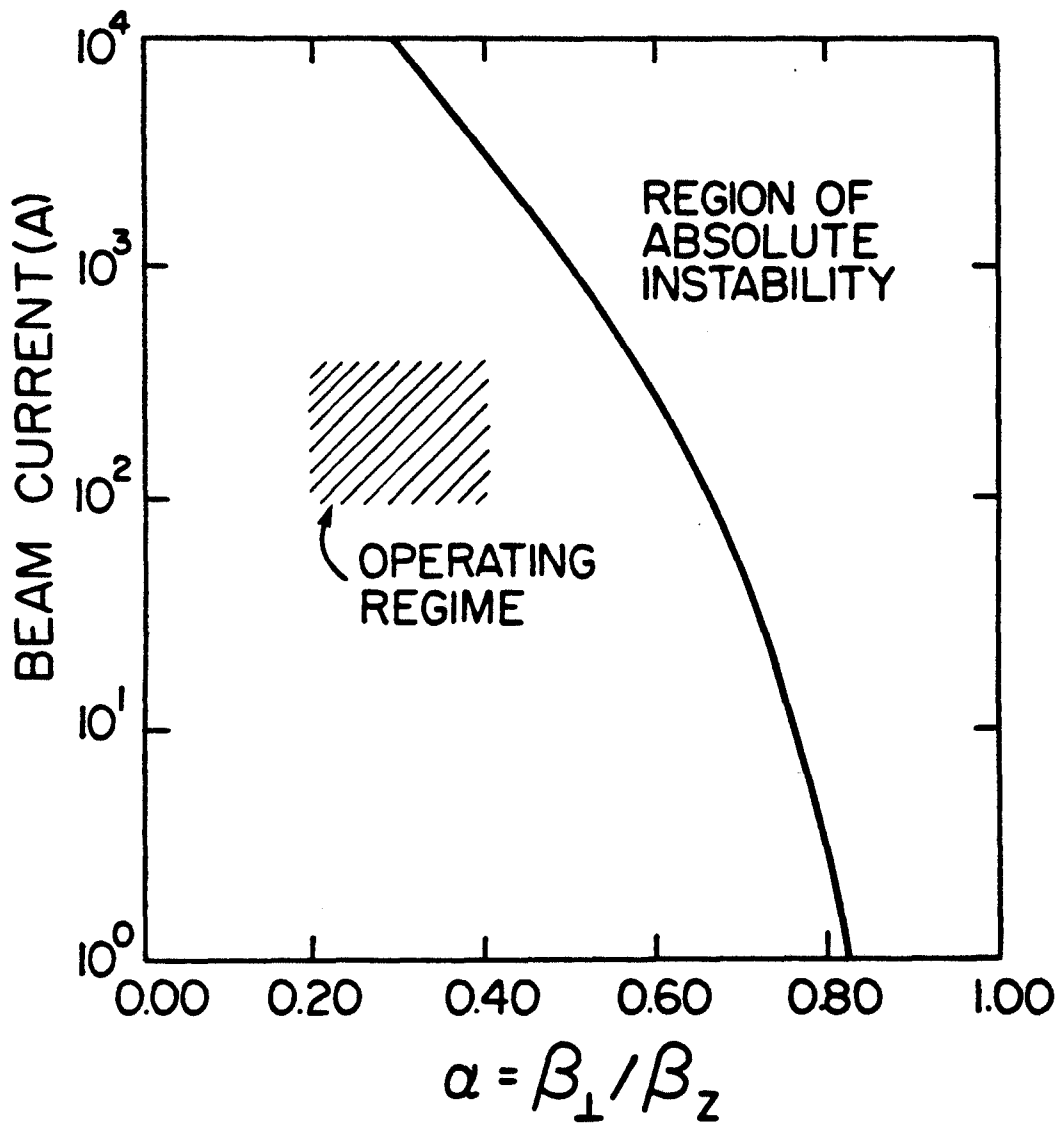
Fig.16. DiRienzo,Bekefi,Chen,
Wurtele

46

Fig.17. DiRienzo,Bekefi,Chen,
Wurtele

47

Fig.18. DiRienzo,Bekefi,Chen,
        Wurtele

48